

## Contents of issue 3–4 vol. LVIII

- 97 J. KALETA, P. WIEWIÓRSKI, *Magnetic field distribution detecting and computing methods for experimental mechanics*
- 119 L.W. MEYER, N. HERZIG, F. PURSCHE, S. ABDEL-MALEK, *Material behavior under dynamic mono- and biaxial loading*
- 131 B.D. KHRISTOFOROV, *Research on influence of impact of microparticles and sewing needles on destruction of solid bodies*
- 139 E. CADONI, A.M. BRAGOV, A. CAVERZAN, M. DI PRISCO, A. KONSTANTINOV, A. LOMUNOV, *Mechanical response of HPFRCC in tension and compression at high strain rate and high temperature*
- 153 S. WOLNY, F. MATACHOWSKI, *Analysis of loads and stresses in structural elements of hoisting installations in mines*

We would like to convey the words of appreciation and acknowledgement to Professor Lech Dietrich, who has been working as the Chief Editor of *ENGINEERING TRANSACTIONS* since 1999. We hardly observed that at the end of this year he is reaching the retirement age and obtaining the status of professor emeritus. We wish Professor Lech Dietrich good health and all happiness and do hope that we can still count on his advice and help in our editorial work.

*Editorial Committee*

## MAGNETIC FIELD DISTRIBUTION DETECTING AND COMPUTING METHODS FOR EXPERIMENTAL MECHANICS

J. Kaleta, P. Wiewiórski

**Wroclaw University of Technology**  
**Institute of Materials Science and Applied Mechanics**

Smoluchowskiego 25, 50-370 Wroclaw, Poland  
e-mail: {jerzy.kaleta, przemyslaw.wiewiorski}@pwr.wroc.pl

This paper presents the design and measuring potential of the latest generation of the magnetic scanner called Magscanner-Maglab System (MMS) which enables a fast acquisition of 3D signals from magnetic sensors and their visualization as digitalized magnetic images for a variety of flat and cylindrical objects. MMS can be used as entirely autonomous or combined (through common control) with a typical material testing machine for static load and fatigue tests. The system can be used to investigate magnetomechanical phenomena and identify their models in experimental mechanics, as well as detect and locate strain fields, areas of plastic deformations and cracks in industrial processes. It has been used recently to measure the magnetic field around objects subjected to technological processing in order to check their quality.

### 1. INTRODUCTION AND RESEARCH OBJECTIVE

Digital visualization is used by various systems (based on discrete sensors or a matrix of sensors) for the human optical perception of real physical effects. Optoelectronic CCD digital cameras or thermal infrared imaging cameras are commonly employed for this purpose. In recent years attempts have been made to visualize the magnetic field by magnetovision cameras. A new NDT/NDE method, called magnetovision, based on such cameras has been developed. The method has found a number of applications in the technology and medicine [1–3]. All ferromagnetic materials can be investigated in this way. The most promising application areas for magnetovision are inverted magnetostriction (also referred to as the Villari effect<sup>1)</sup>) and examination of Smart Magnetic Materials (SMM) [4]. The current research and engineering aim of such experiments is to identify physical models of the Villari effect, which could be used to determine the strain field on the basis of magnetic field strength vector components.

---

<sup>1)</sup>Villari Effect – the effect of mechanical deformation (stretching, twisting, and bending) on the magnetization of a ferromagnetic. Discovered in 1865 by the Italian physicist E. Villari (1836–1904), the effect is the opposite of magnetostriction, i.e., change in the size of a ferromagnetic during magnetization.

The authors' earlier papers presented the foundations of the new diagnostic technique and the possibilities of developing a magnetovision apparatus. They also described the metrological properties of the Villari effect [1, 5, 6] and discussed the possibilities of applying magnetovision in fatigue tests, crack tests [7], and texture tests [8, 9], as well as in athermal martensitic transformations [10, 11].

The development of magnetovision has several limitations whereby it has not been as spectacular as that of thermovision or optoelectronic CCD techniques. The visualization of a scalar quantity, such as temperature, is easy to interpret, whereas the representation of a vector quantity, such as magnetic field strength, in the form of 2D or 3D maps, taking into account the investigated object's geometry, is a much more difficult task. Another difficulty lies in the fact that at the moment no magnetic field sensors in the form of matrices (such as CCD sensor matrices) are available.

Considering the above, a method of measuring the 3D magnetic field in experimental mechanics was chosen as the main objective of this research. In order to achieve the objective the following key tasks were planned:

- developing a non-contact magnetic field strength measurement concept;
- constructing an apparatus (scanner) for investigation of, in particular, flat and cylindrical objects;
- creating a software for measuring, processing and visualization of the magnetic field;
- making identification of magnetomechanical cross effects (the Villari effect) possible;
- providing examples of application of the magnetic field measuring method in investigation of the state of mechanical and SMM objects.

The mentioned above tasks are discussed successively below.

## 2. IDEA OF A NON-CONTACT MEASUREMENT OF THE MAGNETIC FIELD

It was assumed that a magnetic field strength should be measured without any contact with the investigated object. Also, the measurement method should allow one to determine the values of the magnetic field components, respectively  $H_x$ ,  $H_y$ ,  $H_z$ , at different distances  $d$  from the investigated object, starting from very small distances (as small as 0.10 mm). This is vital since as distance  $d$  increases details are lost in the leakage flux above the object. By scanning the plane located at  $d_{\min}$  and performing scans of successive planes distant by  $\Delta d$  from each other, one can determine the magnetic leakage flux over the investigated object and also along the perpendicular axis ( $Z$ ). The idea of the measurement is illustrated in Fig. 1.

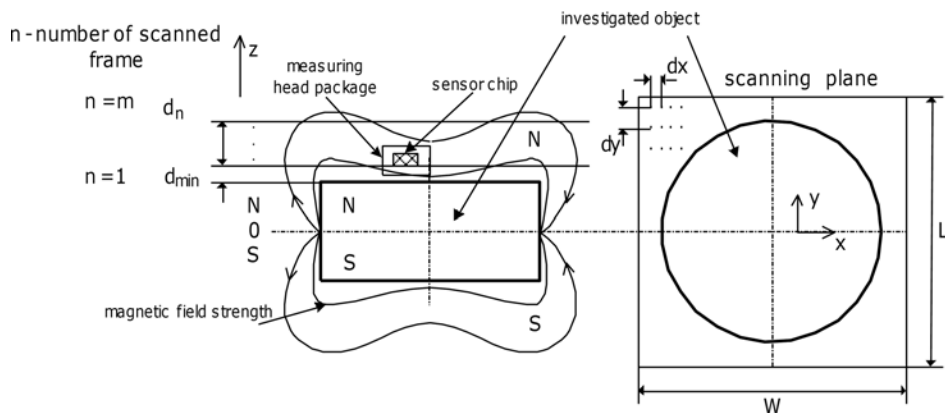


FIG. 1. Scanning with the measuring head with passive sensors to determine the magnetic field strength distribution around the investigated object.

The results of scanning with passive sensors of the plane located at distance  $d$  from the investigated object need to be properly interpreted. In this measurement technique each magnetic field strength reading contains information about the entire geometry of the investigated object. Figure 2 schematically shows the location of the measuring head in space and how its position is ascertained by means of radii  $R_i$  and appropriate angles  $\phi_i$ . Consequently, the two-dimensional map obtained for a given magnetic field vector component is the result of the stereographic projection of the investigated object onto the scanning plane.

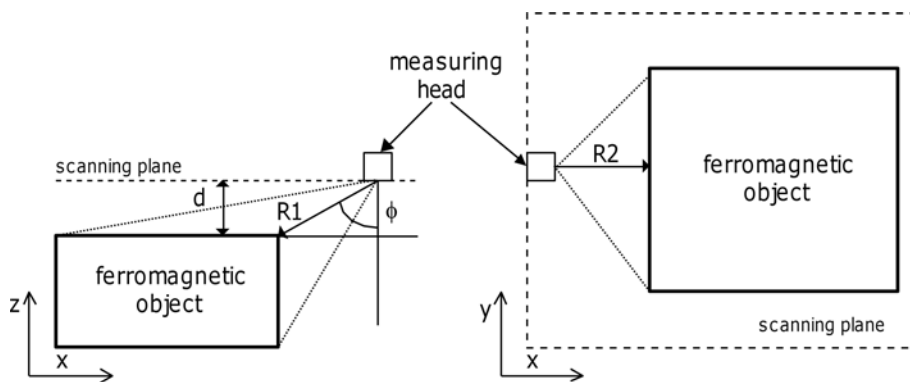


FIG. 2. Scanning of the plane above the investigated object. Interpretation of a 2D map for a given magnetic field vector component, as a stereographic projection of the investigated object onto the scanning plane.

In order to fully investigate the magnetomechanical phenomenon one needs various magnetic field sensors. Passive magnetic field sensors (mainly magnetoresistance sensors and Hall sensors) have been chosen in order to ensure that the magnetic field strength around the investigated object remains undisturbed.

Due to advanced passive magnetic field sensors now all the three components of the magnetic field strength vector can be measured in a single geometric point in space. Since there is a wide range of sensors available, measurements in a wide range of magnetic strength values become possible. The types of sensors used for the particular subranges are:

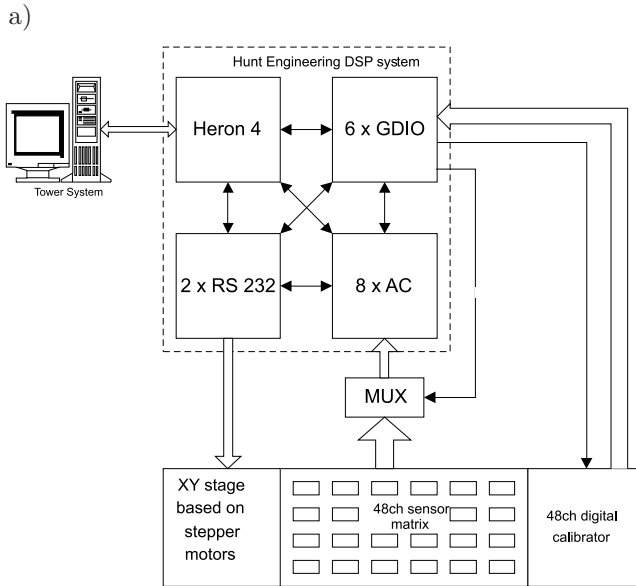
- weak magnetic fields ( $0.1\text{--}100\ \mu\text{T}$ ) – anisotropic magnetoresistance (AMR) sensors;
- medium magnetic fields ( $50\ \mu\text{T} - 10\ \text{mT}$ ) – giant magnetoresistance (GMR) sensors;
- high magnetic fields ( $10\ \text{mT}$  up to  $2000\ \text{mT}$ ) – Hall elements.

Availability of advanced thin-film magnetic field sensors and the introduction of motion processors incorporating a real time operation system (RTOS) have made a 3D visualization of the magnetic field vector by a third generation scanner (magnetovision camera) possible. The scanner features a range of state-of-the-art sensors, software, and mechanical structures. For over a decade the team to which the present authors belong has developed several generations of cameras and scanners which can take magnetic images of materials subjected to various kinds of treatment, mechanic loads, and phase transformations.

### 3. MULTISENSOR MAGNETIC FIELD MEASURING SYSTEM

In the literature one can find solutions which can be used to quickly determine a magnetic field distribution by means of a considerable number of sensors (with identical parameters and characteristics) arranged on a scanning plane [12]. An earlier version of the multisensor magnetovision system recorded magnetic field strength by means of its  $60\times 40$  mm flat measuring head. The solution was based on a system with a digital signal processor (DSP). The measuring unit consisted of a matrix of 48 Philips KMZ52 magnetoresistance sensors. It incorporated analogue and digital circuits shaping the signal and reducing noise as well as ensuring proper data transmission to the signal processing unit. The DSP card, capable of fast data processing and having a large number of input/output interfaces, generated magnetic field maps in real time for two magnetic field components in 24 points. In order to obtain higher resolution maps it was necessary to use an  $XY$  positioner and scanning mode operation.

Figure 3 shows the structure of the magnetovision system. A Hunt Engineering HERON card incorporating a C6701 digital signal processor forms its signal processing unit. Conversion of measurement data into the digital form and their final processing is the task of this part of the measuring system. Signal processing is understood here as digital processing of signals, i.e., decoding, digital filtration, and Fourier transformation.



b)

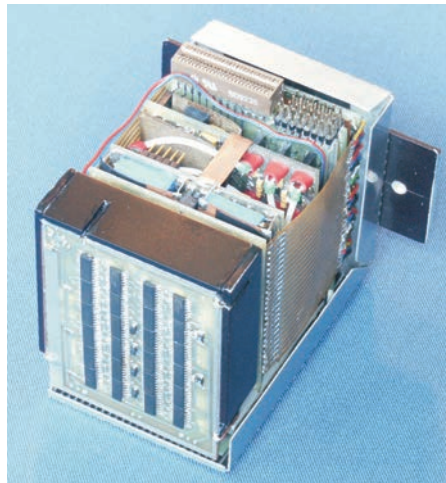
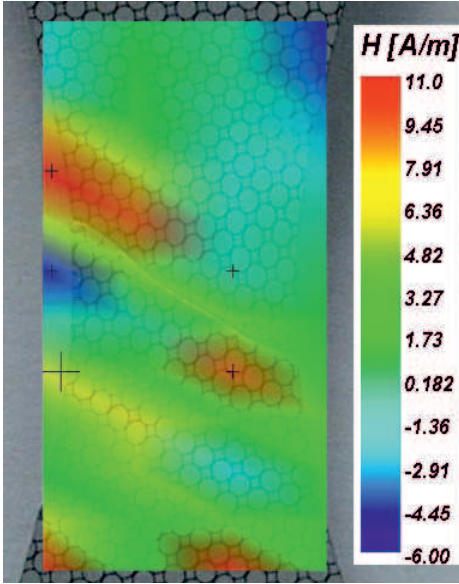


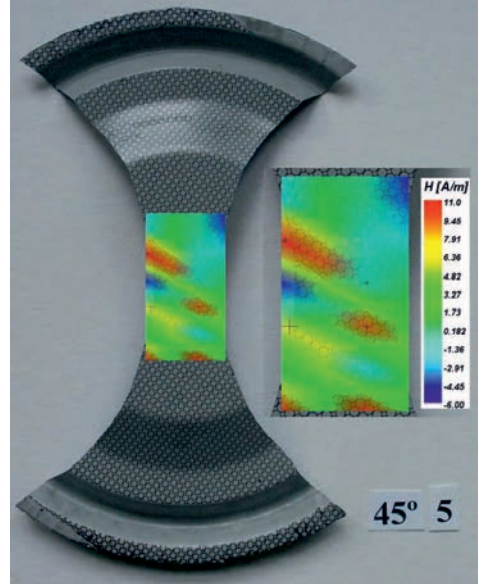
FIG. 3. Multisensor magnetovision system: a) system structure, b) measuring head with 48 magnetic field sensors.

The above system was used mainly to monitor metal sheet forming and to determine the formability of metal sheets and the texture of the material [8, 9]. Figure 4 shows exemplary results of monitoring the metal sheet forming process and determining the loss of stability by the metal sheet. The experience gained in the building of the system was then used to create magnetic field scanning devices based on 3D sensors.

a)



b)



c)

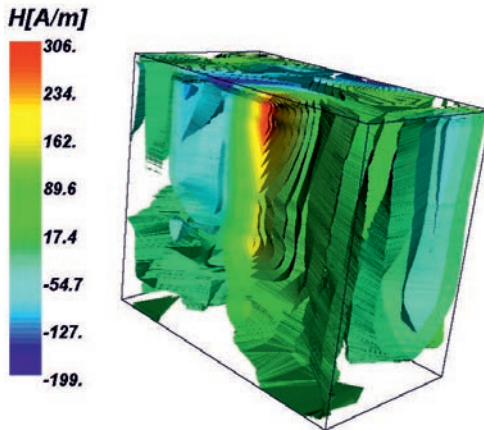


FIG. 4. Exemplary results of monitoring a metal sheet forming process and determining the loss of stability by a metal sheet: a) magnetic field map superimposed on the crack area, b) die stamping with a crack, c) isosurfaces of the magnetic field variation during the forming.

#### 4. MAGNETIC FIELD SCANNER AND THE INVESTIGATION METHODOLOGY

The main components of the magnetic field scanner and its software, as well as exemplary applications of the measuring system in experimental mechanics, are presented below.

#### 4.1. Scanner design

The main objectives achieved in the Magscanner system project are:

- a mobile modular measuring system;
- a wide programmable range of mechanical movements of the movable part incorporating a measuring head;
- scanning parameters, i.e., the set position and scanning speed, controlled by a motion processor based on RTOS;
- the measuring head (an autonomous part of the system) is a complete analogue measuring circuit which can be replaced with another one with different specifications;
- all scanning operations are controlled by a single dedicated software.

A block diagram of the Magscanner system is shown in Fig. 5. The control unit of Magscanner consists of the following components (Fig. 5a):

- an IBM T30 computer with a docking station using a PCI control card to serve all Magscanner operations;
- an advanced motion control system APCI-8001 by ADDI-DATA. The motion controller incorporated in the APCI-8001 controls scanner precision positioning and ensures its optimal dynamics;
- a sensor signal acquisition system based on DT9804 by Data Translation, with a digital trigger to synchronize carriage positions and analogue values from the sensors;
- software dedicated to Magscanner/Maglab, controlling the whole system and visualizing the results. A lot of effort has been put into the development of this software. Recently the part responsible for further processing of the results has been separated from Magscanner and called Maglab. This software package enables export of the results to CAD systems and visualization of the magnetic field vector in a 3D space.

The Magscanner system has been adapted to perform several tasks in the field of experimental mechanics. Now this magnetovision system has four independent magnetic inspection subsystems (shown in Fig. 5b):

- an advanced XYZ scanner which can work in tandem with material testing machines (MTS). The guaranteed resolution of the measuring head travel is 2160 DPI. In terms of functionality, the measuring head's positioning system is based on the same principle as the professional A3+ format scanners, e.g., the AGFA DuoScan series. The working scanning range is  $410 \times 180 \times 200$  mm. The  $Z$  axis enables performance of a series of scans for a set distance from the investigated object, and it is also needed to install the system on a strength testing machine in order to

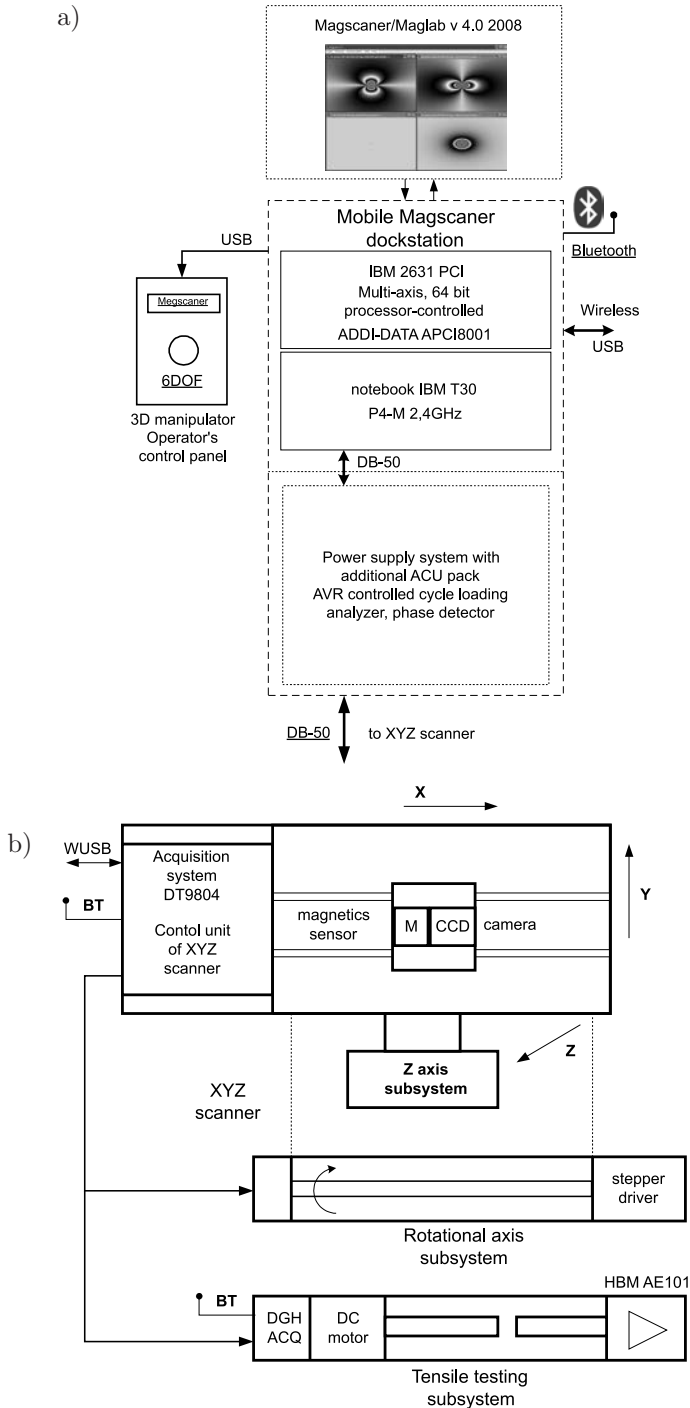


FIG. 5. Block diagram of the magnetic field scanner: a) computer-aided system, b) subsystems: XYZ scanner, rotational scanner, tensile testing machine.

acquire maps of magnetic field distribution maps from, e.g. a fatigue process;

- measurement heads based on:
  - Honeywell HMC1053 – for WMF and MMF;
  - Allegro Micro RMT34 Hall elements – for HMF;
- a rotational axis analyzer – a subsystem designed for measuring and analyzing magnetic field distribution around axisymmetrical elements (e.g., cylinders and pipes), mainly with quick industrial tests in mind. The al-

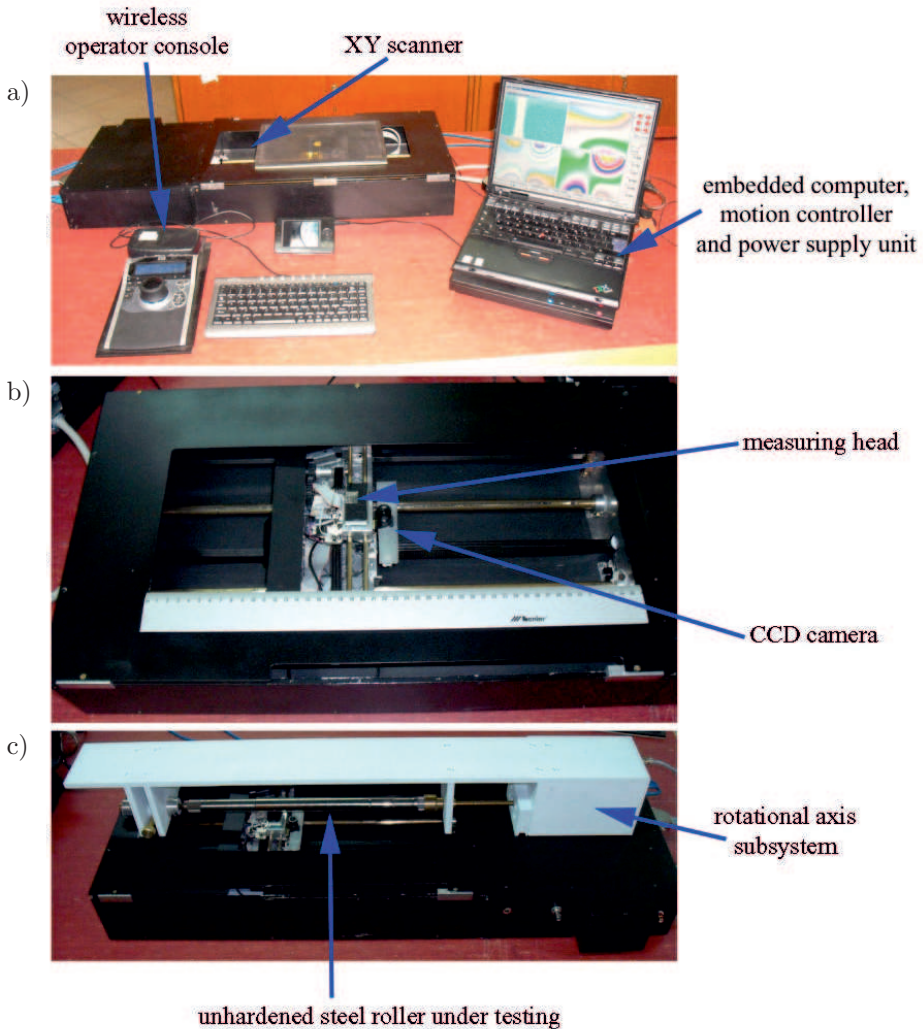


FIG. 6. Magscanner system: a) scanner setup, b) XY scanner, c) scanner for axisymmetrical objects.

gorithm can be used for testing of magnetic and electrostatic cylinders in refabrication of toner cassettes for laser printers. Currently, research on potential applications in the car industry is being conducted;

- a micro-tensile testing machine – a device enabling precise measurements of the magnetic field and mechanical quantities for foil materials subjected to static strength tests. The beam scanning movement resolution is 0.25 micrometers. The force of 1.0–500 N can be measured thanks to an HBM AE101 amplifier (class 0.1%).

All the subsystems are controlled by the same control unit and by the Magscanner software. The magnetovision scanner and its components are shown in Fig. 6.

Figure 6a shows the magnetic scanner setup. One of the major advantages of the system is its mobility. The number of cables has been reduced to an absolute minimum. A wireless operator panel (based on the wireless USB standard) has been introduced. The main scanner functions can be controlled from the panel. Figure 6b shows the measurement zone of the XY scanner including a measuring head and a CCD camera for recording the scanning of the investigated object. In order to illustrate the capabilities of the Magscanner, the way of setting up the subsystem for scanning cylindrical objects is shown in Fig. 6c.

#### *4.2. Scanner measuring specifications*

The main specifications of the Magscanner system and its subsystems are as follows:

- range of magnetic field measurement at 16 bit ADC resolution:
  - WMF: a 0.1–100  $\mu\text{T}$  AMR head based on the Philips KMZ5x series MR,  
a 1.0–500  $\mu\text{T}$  AMR head based on a modified Honeywell HMC105x series MR;
  - MMF: a 50  $\mu\text{T}$  – 10 mT AMR head based on the Philips KMZ1x series MR,  
a 1–100 mT head based on Hall elements by Allegro Micro;
  - MMF/HMF: a 20–2000 mT head based on RMT34 Hall elements by Allegro Micro;
- max. scanning speed – 50 000 points/sec;
- max. scanning resolution – 2160 DPI (0.02 mm);
- max. number of scanned magnetic field points – 20 million points (maps as large as 20000 $\times$ 1000);
- DT 9804 card sampling frequency at 16-bit resolution – 100 kHz.

### 4.3. Preparation of measuring heads

The measuring heads are decisive for achieving a satisfactory magnetic field measurement quality. There is no universal measuring head which could be used for measurements in the whole magnetic field range. Also, the size and shape of the head depend on the peculiarities of the investigated object and on the number and size of the sensors used. A head for measuring flat surfaces will be different from the one for determining a magnetic field distribution on cylindrical surfaces. In a triaxial head the three magnetic field sensors perpendicular to each other should be located possibly in one point in space. For example, an integrated Hall probe was made by sticking together three Hall sensors (for  $H_x$ ,  $H_y$  and  $H_z$ , respectively), each with their own independent conditioning system. Due to the small dimensions of the Hall-effect magnetic field measuring system ( $3 \times 3 \times 2 \text{ mm}^3$ ), quasi-point measurements (necessary in the case of cylindrical surfaces) can be performed. A special head based on Honeywell HMC1053 magnetoresistors was developed for the triaxial measurement of the magnetic field vector on a flat surface. Measurements can also be made using a head based on Philips KMZ52 or KMZ51 magnetoresistors.

### 4.4. Maglab software – a complete tool for magnetomechanical evaluation

Maglab software is a major component of the Magscanner system. The proposed method of evaluating the magnetic field distribution around different objects is based on modified passive sensors made by Honeywell and on the dedicated Magscanner/Maglab software which is compatible with industrial parametric CAD systems (e.g., ProEngineer and Solid Works) and with NURBS (Rhinoceros). The measurement technique consists in acquiring a set of points belonging to equally distant planes, similarly as in tomography and 3D visualization in CAD under the IGES standard.

The possibilities offered by the Magscanner-Maglab systems are presented below. Two aluminium plates (discs) with circular holes aligned in parallel were the test objects. The plates that were connected to a power source were subjected to a quasistatic tension until rupture. The direction of the current (reverse in both plates) is shown in Fig. 7. Such a process, combining both the mechanical and electrical loadings of the plates, is hard to describe analytically. Visualization of the magnetic field with the use of commercially available systems is difficult or even impossible.

Figure 8 shows Maglab windows with magnetic field strength distribution maps before uniaxial tension and immediately after the failure of a set of two plates with holes. As the plates were under tension, a current of 1 A was flowing through them. Figure 8a shows the image from the photodiode (PD; the geo-

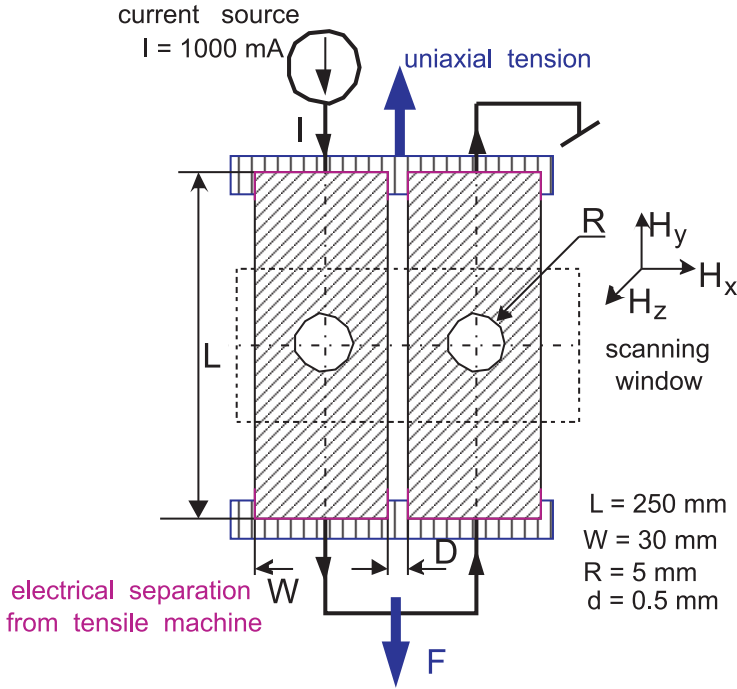


FIG. 7. Scheme of the uniaxial tension of the aluminium plates connected to a power source.

metric resolution is identical to the resolution of the magnetic sensors) and the distribution of the  $H$  vector components, marked subsequently as  $H_y$ ,  $H_z$ ,  $H_x$ . To the right, the courses of these quantities are presented for the cross-section drawn through the middle of the holes. Analogous characteristics for the final phase of the sample rupture are shown in Fig. 8b. Additionally, the embedded colour scheme generator is presented in Fig. 8c.

The main features and modules of the Maglab software are as follows:

- four windows: MagnX, MagnY, MagnZ, showing (with a set resolution) the distribution of the three magnetic field vector components in the scanned area, and the Camera window showing a map received from an optical sensor;
- the possibility of a simultaneous work on 10 different projects stored in the clipboard for comparisons and further analyses;
- high resolution of the maps, dependent on the sensor distance from the investigated object;
- the possibility of displaying multiframe projects a movie;
- a built-in module for creating and selecting the best spectrum of colours (the Pattern of colours in Fig. 8c) to represent the determined distributions;

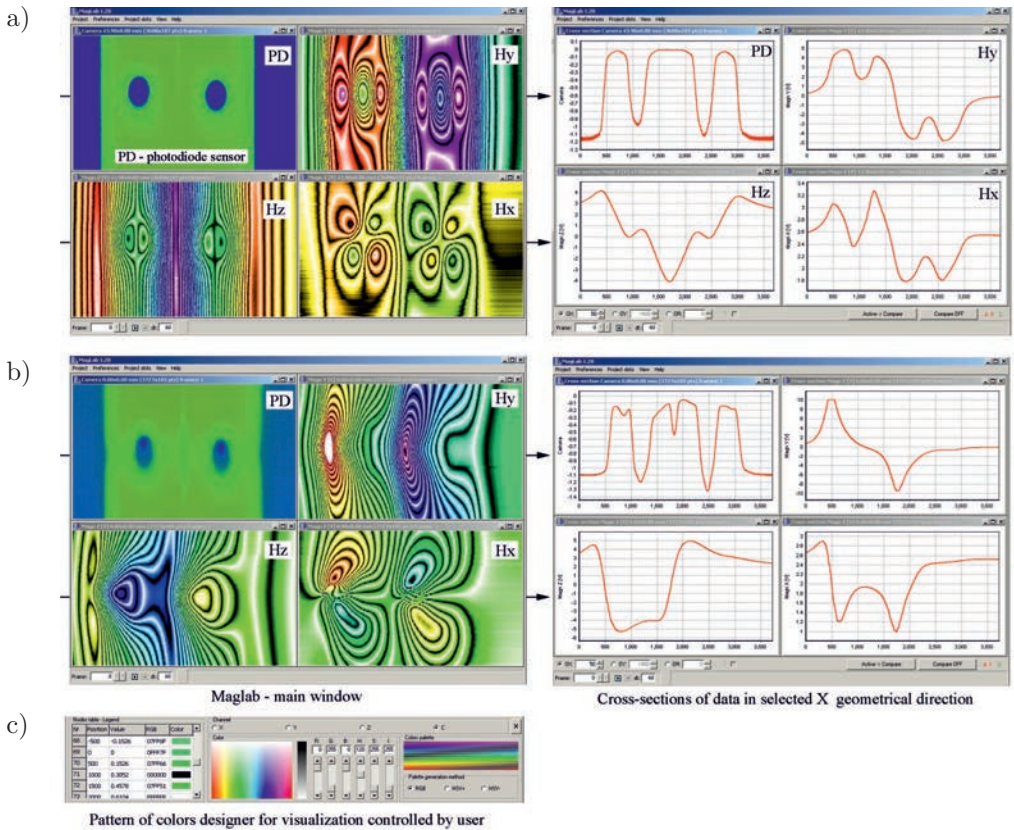


FIG. 8. Features of the Maglab software for the sample subjected to tension and connected to a power source (as shown in Fig. 7).

- a sensor position correction module enabling fitting of the maps that come from the sensors located in different points;
- a Cross sections module enabling the user to create and edit linear cross sections from the acquired maps;
- a Hysteresis module enabling generation of waveforms in specified coordinates and time domain;
- the Magscanner/Maglab software package enables further processing and visualization of the magnetic field distribution maps in a CAD program (ProEngineer) or in NURBS (Rhinceros);
- Maglab allows one to quickly generate maps of the stress distribution, strains, and the specific energy for the Kirsch problem.

In addition, Maglab has basic magnetostatic models implemented as standards for experimental measurements. Strong emphasis has been placed on the way results are presented and on optimization of calculations. Therefore, the

software package can find many applications also in other areas requiring knowledge of magnetic field distribution. In the nearest future, the main application area will be identification of magnetomechanical dependences for a plate with a central hole subjected to fatigue.

Due to visualization of an elementary magnetic field vector distribution as a stereographic projection [13] it was possible to develop the Dipole Contour Method (DCM) which has been implemented in the Magscanner-Maglab software package [14]. The concept of DCM and other related notions shown in Fig. 9. This method is used to visually represent information supplied by data.

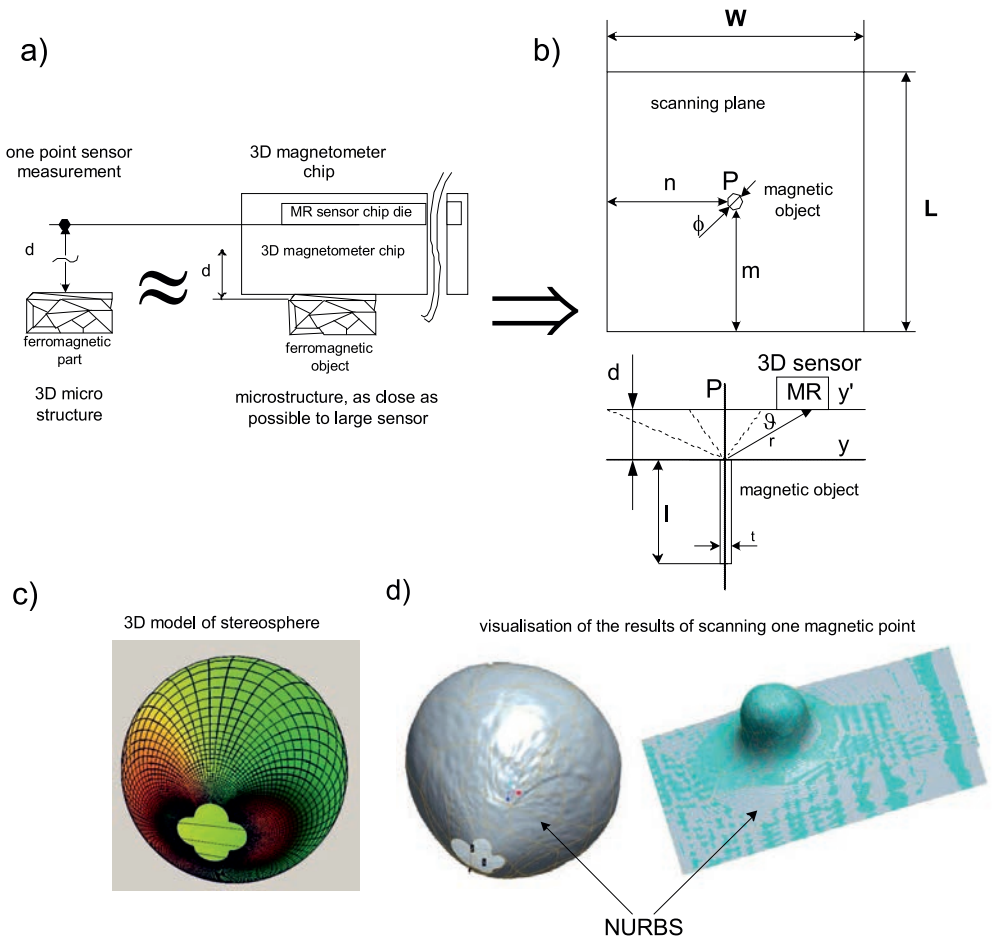


FIG. 9. Magnetic field distribution as a stereographic projection [14]: a) distance  $d$  and sensor chip are not small enough to measure elementary micromagnetism, b) single point magnetic object produces stereographic projection, c) stereosphere obtained from the model and from the experiment (d) as a flat area magnetic field distribution. It should be emphasized that the stereosphere from the experiment was created with the use of many NURBS surfaces.

Since due to its size the chip with sensors cannot take precise point measurements, dipole contouring is necessary to:

- find the location of the zero line field in the axially symmetrical roller;
- locate polarity zones between different materials;
- determine the magnetomechanical effect;
- track the movement of the actuator rod;
- trace the magnetic field distribution at a required distance.

An isopleth is an equal value line, and dipole contouring consists in plotting magnetic isopleths similar to a weather map.

Presentation of the Maglab software package, either as autonomous or working with material testing machines, would extend far beyond the confines of this paper. Therefore, only a few selected applications of the software are presented below.

#### *4.5. Application of the Magscanner-Maglab system to identify the Villari effect*

Identification of an inverse magnetostriction (the Villari effect) for a plate with a circular hole (the so-called Kirsch specimen) subjected to cyclic loading is described in several papers [1, 5, 6, 15]. Such identification would make it possible to use a magnetic field image to describe the state of strain of a material and even the strain field in structural nodes made of ferromagnetic materials. However, there is a problem with a sufficiently precise local non-contact measurement of the magnetic field for different Kirsch specimen loading configurations. It should also be possible to generate a magnetic field image depending on the adopted magnetomechanical model of the Villari effect. Therefore, the Kirsch problem has been implemented in the Maglab software package whereby it becomes possible to determine the theoretical distribution of:

- a 2D state of stress;
- a 3D state of strain;
- specific energy;
- stress tensor axiator and deviator components.

The Maglab application can simulate the cyclic loading of the Kirsch specimen only in the elastic region for the selected geometry, which is signalled in the application. Using the elementary magnetomechanical models described in [6] and the Dipole Contouring Method one can obtain a 3D magnetic field distribution, also inside a hole, taking into account the edges of a sample. Figure 10 shows the Maglab windows used for defining the initial parameters and selecting the magnetomechanical model of the Kirsch specimen. In Fig. 10 no magnetic field strength  $H$  scale is given because the representation of  $H_x$ ,  $H_y$ ,  $H_z$  distributions around the hole for selected  $\sigma_{EF}$  models is of central importance.

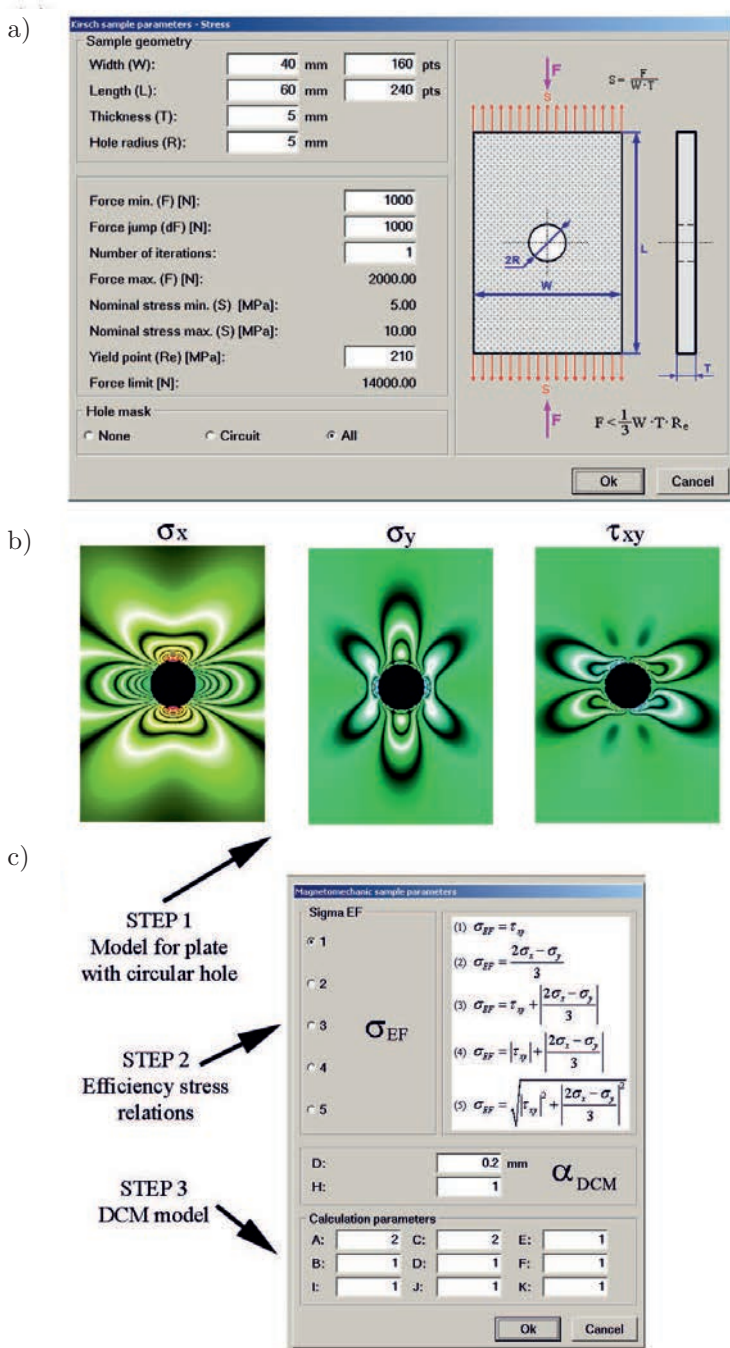


FIG. 10. Implemented DCM model for the plate with a circular hole (Kirsch specimen): a) the parameters of the sample geometry and loading selected to generate the stress distribution, b) the obtained stress distribution, c) selection of the magnetomechanical model [6, 16] and DCM parameters.

Figure 11 shows magnetic field distributions based on models 1, 2 and 5 [16].

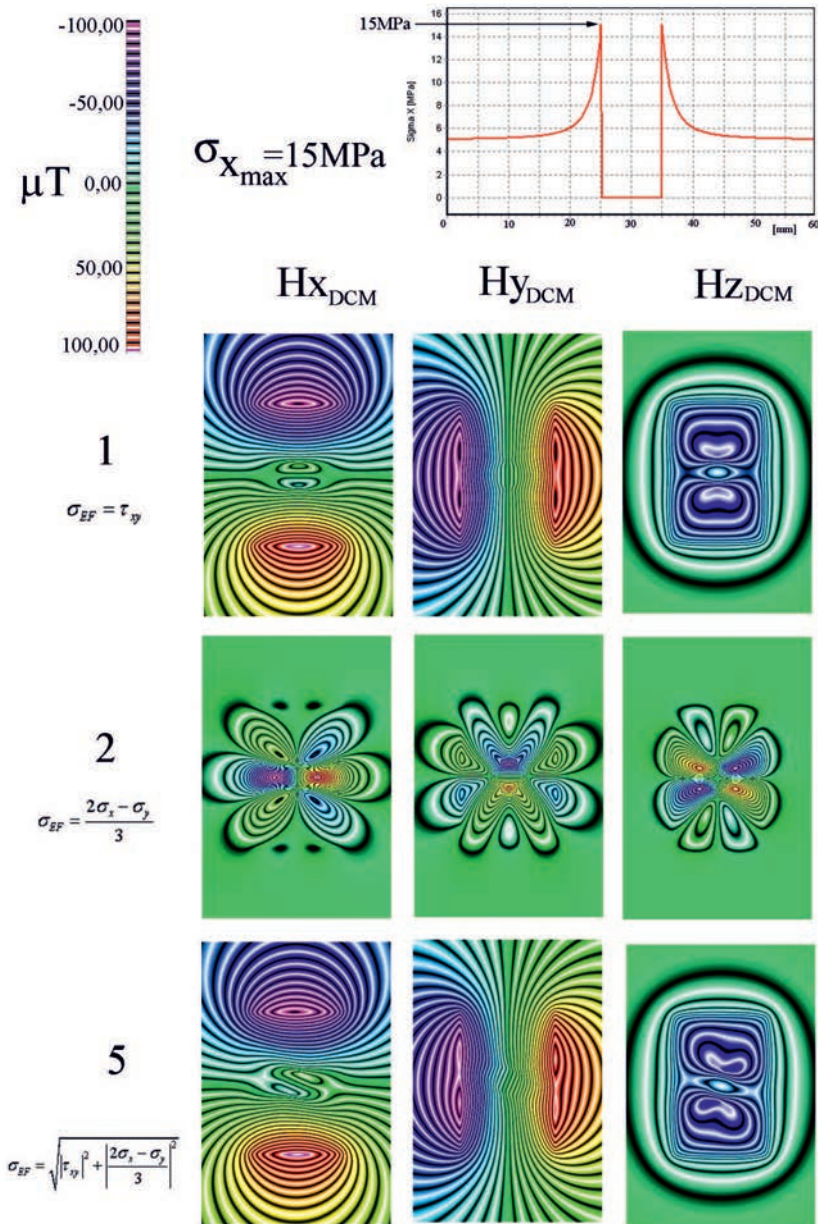


FIG. 11. Shapes of the magnetic field distributions around a circular hole in the loaded Kirsch specimen, computed in Maglab using the magnetomechanical models [16] and DCM.

The Magscanner-Maglab system uses a point-by-point scanning algorithm with simultaneous recording of the full loading period divided into a fixed num-

number of frames in order to determine the magnetic field distribution around a circular hole in a real Kirsch specimen subjected to cyclic loading.

Currently, the Magscanner-Maglab system can record periodic changes in the magnetic field around flat and cylindrical surfaces in the frequency range of 0.1–200 Hz at the resolution of 1/360. Thus, for repeatable conditions in the whole scanning range it is possible to produce maps of the magnetic field in a particular synchronizing signal phase. Cyclic loading of materials in the elastic range satisfies such requirements. Then the variable magnetic signal component is the Villari effect model.

Figure 12 schematically shows the point-by-point scanning algorithm and the generation of four maps, each with 360 frames or a prescribed number of frames. The current system can repeat point-by-point scanning after a break lasting a prescribed number of synchronization run periods. The box marked as ‘C’ (other sensor type) means that there is a possibility of using, for example, a photodiode.

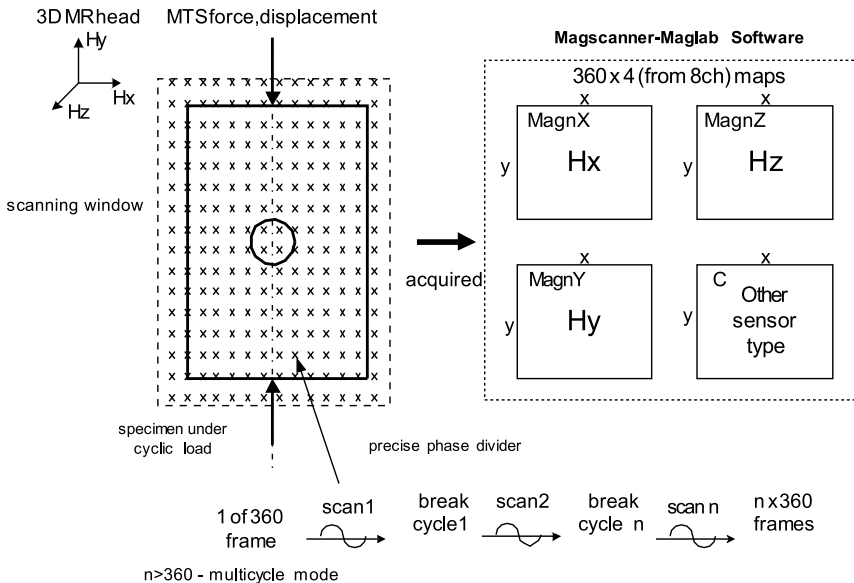


FIG. 12. Method of observing magnetic field vector aberration during a fatigue under a sinusoid loading.

Figure 13 shows the magnetic field distribution around a plate with a circular hole subjected to a symmetrical cyclic loading in three display modes: “RGB” – colours from the RGB palette are assigned to the magnetic field values, Isopleth – colours are separated by alternately black and white (creating the impression of contour lines on a map), and “AC” – the differential frame between the reference frame (reference phase of the signal) and all the recorded frames.

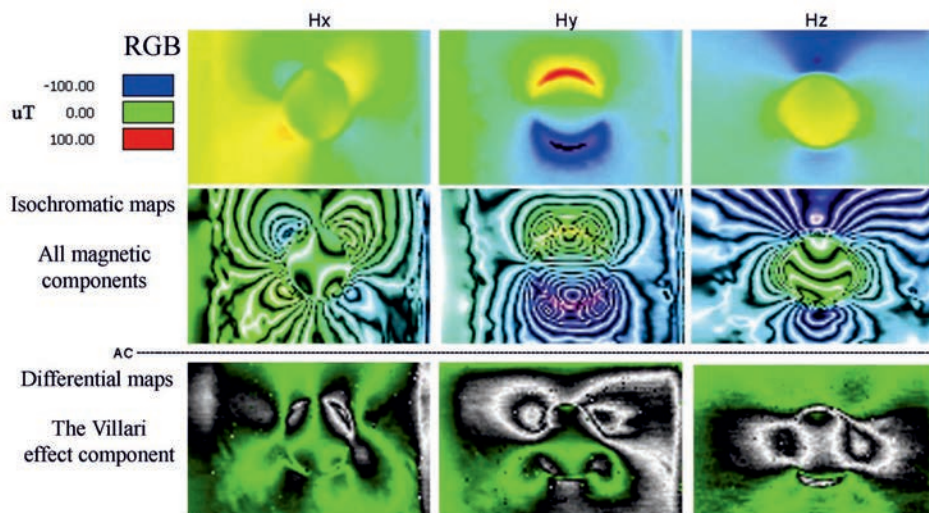


FIG. 13. Magnetic field distribution around a Kirsch specimen under a fatigue process, presented in three different modes of maps: RGB, isochromatic and differential isochromatic.

Consequently, a magnetic field distribution being solely the result of the Villari effect is obtained.

## 5. OTHER SELECTED APPLICATIONS

Exemplary applications of the scanner, featuring an earlier version of the magnetovision camera can be found in the papers [1, 4, 7–11, 14, 17] by the authors. New applications of the magnetovision system are connected with measuring the magnetic field around objects subjected to technological processing (cutting, laser ablation, electro-discharge drilling, micro-layer plotting, magnetic printing, etc.) in order to check their quality.

Figure 14 shows two such applications from the authors' independent experiments [18]. In the a) case it is the optical and magnetic image of the text which was laser engraved on steel. In the b) case the magnetic image of a letter 'A' sign on a disc is shown.

The Magscanner/Maglab (2010) system in its current version is a complete tool for magnetic investigations in mechanics. The system is capable of analyzing fatigue processes at low load frequency (up to 200 Hz) and registering the magnetic field vector in one degree steps (animated movie with 360 magnetic frames). Also, a handheld 3D digitizer for monitoring magnetic field strength has been designed, and its prototype has been built. The handheld wireless magnetoscanner incorporating a precision movement recorder is compatible with the Magscanner software and the other subsystems. The data acquisition unit is contained in the small Razer Lachesis computer mouse casing.

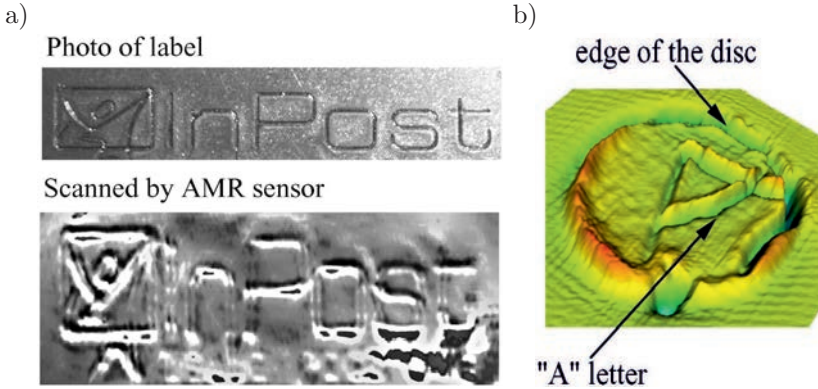
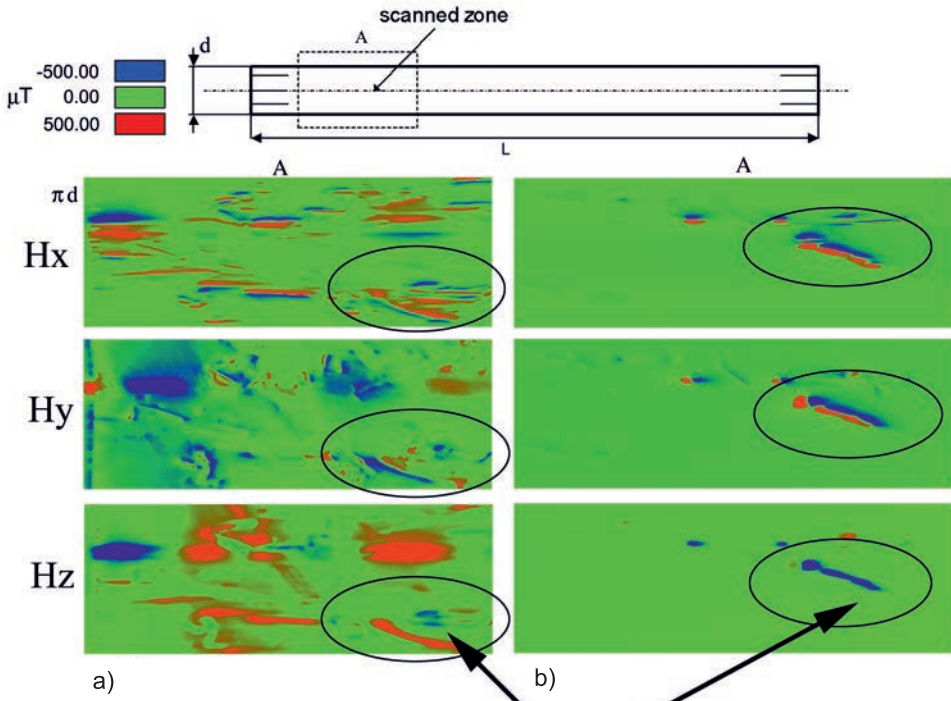


FIG. 14. Magnetic field strength disturbance used to detect changes on a ferromagnetic's surface: a) laser engraving, b) letter A sign on a disc [18].

The Magscanner/Maglab system can be used to control the quality of inductive hardening. Figure 15 shows magnetic field distributions on the cylindrical surface of a car axle shaft. The “Critical Zones” are specified as zones which run



Critical Zones as residual magnetic field distribution after induction hardening

FIG. 15. Rotational axis subsystem used for magnetic inspection of a car axle shaft: a) unhardened and b) after induction hardening.

the most risk of improper hardening, which shows itself in the larger range of magnetic field values close to the surface compared to the average distribution of the magnetic field on the shaft. Due to the use of the system a “Critical Zone” of the axle shaft can be controlled for improving the quality of inductive hardening.

## 6. CONCLUSIONS

1. A new generation of magnetic scanner for investigating various problems in experimental mechanics has been presented. The scanner enables the simultaneous determination of three magnetic field strength components  $H_x$ ,  $H_y$ ,  $H_z$  for flat and cylindrical objects. The non-contact measurement takes place at a set distance  $d$  from the investigated surface.
2. The measuring system is equipped with the Magscanner/Maglab software which enables signal acquisition, processing and visualization, also with the use of the Dipole Contour Method (DCM).
3. The possibilities of using the measuring system to identify the Villari effect model have been demonstrated for a plate with a circular hole subjected to cyclic loading.

Considering the above, it can be stated that the research objective has been achieved.

## REFERENCES

1. J. KALETA, *Magnetomechanical Effect in Fatigue Investigations of Ferromagnetics*, Proc. of EUROMAT-2000, **2**, 1149–2254, 2000.
2. S. TUMANSKI, A. LISZKA, *Magnetic sensor array for investigations of magnetic field distribution*, J. Magn. Magn. Mat., **242–245**, 1253–1256, 2002.
3. C. H. SMITH, R. W. SCHNEIDER, M. TONDRA, *Biosensors: a New Use for Solid-State Magnetic Sensors*, Sensors Magazine, **16**, 12, 14–20, 1999.
4. J. KALETA, P. WIEWIÓRSKI, *Wireless 3D Magnetic Field Digitizer for inspection of parts fabricated using Smart Magnetic Materials*, Proc. of IV ECCOMAS Thematic Conference on Smart Structures and Materials, Porto, 2009.
5. J. KALETA, P. WIEWIÓRSKI, *Magnetovision as a Tool for Investigation of Fatigue Process of Ferromagnetics*; Proc. of Fatigue 2001, Sao-Paulo, December 12–14, 2001; 7, 2001.
6. J. KALETA, R. GÓRECKI, *Method of visualizing cross fields in plates subjected to cyclic loading. Fatigue and fracture mechanics* [in Polish], Proc. of XIX Symposium on Fatigue and Fracture Mechanics, Bydgoszcz, 2002.
7. J. KALETA, P. WIEWIÓRSKI, *Detection of defects in magnetic composite rods by means of high-resolution scanner* [in Polish], Acta Mechanica et Automatica, **1**, 1, 39–44, 2007.

8. J. KALETA, P. WIEWIÓRSKI, W. WIŚNIEWSKI, *Examination of texture of ferromagnetic sheets, using the Villari effect* [in Polish], Symposium on Mechanics of Failure of Materials and Structures, Augustów, 2003.
9. J. KALETA, P. WIEWIÓRSKI, W. WIŚNIEWSKI, *Magnetic memory of ferromagnetic material deformation history* [in Polish], Proc. of IX Domestic Conference on Fracture Mechanics, Kielce-Cedzyna, 14–17 September, 2003, Wydaw. P. Świętokrz., pp. 221–228, 2003.
10. B. FASSA, J. KALETA, P. WIEWIÓRSKI, *Methodology of investigating athermal martensite transformation in austenitic foils* [in Polish], Proc. of XIX Symposium on Fatigue and Fracture Mechanics, Bydgoszcz, 2002.
11. B. FASSA, J. KALETA, P. WIEWIÓRSKI, *Martensite transformation induced by plastic strain in foils made of metastable austenite* [in Polish], Proc. of VIII Domestic Conference on Fracture Mechanics, Kielce-Cedzyna, September 17–19, 2001; 8, Kielce, 2001.
12. S. TUMANSKI, S. BARANOWSKI, *Magnetic sensor array for investigations of magnetic field distribution*, J. Electr. Engin., **57**, 8/S, 185–188, 2006.
13. P. P. HORLEY, V. R. VIEIRA, P. D. SACRAMENTO, V. K. DUGAEV, *Application of the stereographic projection to studies of magnetization dynamics described by the Landau–Lifshitz–Gilbert equation*, J. Phys. A: Math. Theor., **42**, 315211 (11 p.), 2009.
14. J. KALETA, P. WIEWIÓRSKI, *The Dipole Contouring Method as a tool for magnetic field distribution in premagnetization zone in SMART actuator*, Proc. of IV ECCOMAS Thematic Conference on Smart Structures and Materials, 2009.
15. YANG EN, LI LUMING, CHEN XING, *Magnetic field aberration induced by cycle stress*, J. Magn. Magn. Mat., **312**, 72–776, 2007.
16. M. J. SABLİK, *Modelling the effects of biaxial stress on magnetic properties of steels with application to biaxial stress NDE, DPA*, Amsterdam, 1995.
17. J. KALETA, D. LEWANDOWSKI, P. WIEWIÓRSKI, *3D magnetovision scanner as a tool for investigation of magnetomechanical principles*, Solid State Phenomena, **154**, 181–186, 2009.
18. J. KALETA, P. WIEWIÓRSKI, *Construction of magnetic scanner for application in experimental mechanics*, Proc. of 26th Danubia-Adria Symposium on Advances in Experimental Mechanics, pp. 95–96, Leoben, September 23–26, 2009.

## MATERIAL BEHAVIOR UNDER DYNAMIC MONO- AND BIAXIAL LOADING

L. W. Meyer, N. Herzig, F. Pursche, S. Abdel-Malek

**Nordmetall GmbH**

Hauptstrasse 16, D-09221 Adorf/Erzgebirge, Germany

This paper gives an overview of different testing methods and the mechanical material behavior including mono-axial and multi-axial testing under high rate loading. Special emphasis is laid on difficult loading conditions and loading states such as a high temperature and high strain loading ( $\vartheta > 1200^{\circ}\text{C}$ ,  $\varphi > 1$ ) and multiaxial impact tests. The impact behavior of selected materials is shown and compared for different loading conditions. Furthermore, a distinction is made between virgin and manufactured material behavior (e.g. welding) or pre-damaged materials. Specifically, if the influence of the manufacturing history is investigated. Under certain loading states the impact material properties show a dramatic difference compared to the virgin state of the material. Some examples of different material behavior under the conditions previously mentioned are given.

### 1. INTRODUCTION

It is well-known, that the material behavior of construction materials is dependent on strain, strain rate and temperature. Moreover, the knowledge of the dynamic behavior of materials is of interest, if such processes like cutting or forming operations are investigated. For many engineering applications, the mechanical impact behavior of materials and components also play an essential role.

For example, consider a deployed naval ship operating in rough sea conditions: the loading of this ship's structure by a canon fire can be described as a time-dependent strain loading (Fig. 1). In reality, the loading is measured by strain gages. If the amplitude of the strain-time signal is multiplied by Young's modulus (Hooke's law), one may find a stress value significantly exceeding the material flow stress as known from quasistatic and standardized experiments. Hence, if the assumption is valid, the ship must be deformed plastically. However, an examination of the strain-time signal shows a complete return to its initial state, which clarifies that the whole event was purely elastic. Investigations under dynamic tensile loading, using a universal hydraulic testing machine, show that the large strain-rate sensitivity of the flow stress of the ship building steel, during the impact by canon firing, is enhancing the flow stress above that

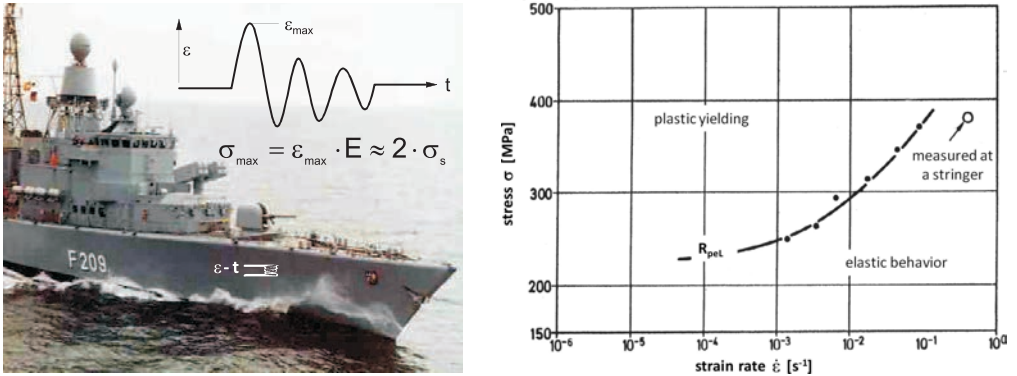


FIG. 1. Dynamic loading of a canon shooting on a Navy ship structure.

(elastic) value, what was measured on the stringer at the high strain rate. Thus, the ship is not being deformed plastically during maneuver operations or its deployment.

However, the knowledge of the material behavior under loading conditions matching the intended use, is of special importance in design and construction. Thereby, the material behavior must be known over a wide range of strains, strain rates and temperatures. A variety of different experimental techniques exist to determine the dynamic behavior of materials under the defined loading conditions and loading states.

## 2. IMPACT TESTING CAPABILITIES

Of the experimental work on impact material behavior described in the literature, mostly the Hopkinson bar testing is mentioned. However, a variety of different experimental techniques exist to determine the dynamic behavior of materials under the defined loading conditions and loading states.

For characterization of the mechanical behavior of material investigations over a wide range of strains, strain rates and temperatures are required. Additionally, different loading types may lead to different material behavior, even if only monoaxial loading is mentioned and must be considered in material investigations and constitutive modeling. In Fig. 2, a summary of different loading types under monoaxial and multiaxial loading is given.

For dynamic impact testing of materials, only a small amount of universal testing machines in comparison to quasistatic loading is available. Especially, accurate force-time measurements are a great challenge for such type of machines. Due to the large mass, which has to be accelerated during testing, the force-time signals often show large ringing and lead to increased uncertainties in

loading type / strain rate [ $s^{-1}$ ]		$10^{-3}$	$10^{-2}$	$10^{-1}$	$10^0$	$10^1$	$10^2$	$10^3$	$10^4$	$10^5$	temperature [°C]
uniaxial stress / strain	tension	■	■	■	■		■	■			-190 ... 1250
	compression	■	■	■	■		■	■	■		-190 ... 1250
	torsion	■	■	■	■		■				-190 ... 1100
	bending	■	■	■	■		■				-190 ... RT
	shear	■	■	■	■	■	■				RT
biaxial stress / strain	servohydraulic (tension, compression + torsion, TU Chemnitz)	■	■	■	■						-190 ... 400
	drop weight (compression + shear)						■	■	■	■	-190 ... 1200
	gas gun (compression + shear)							■	■	■	RT
	drop weight – blast simulator				■	■	■				RT
	hopkinson (tension + torsion)					■	■				RT
	charpy Impact test						■	■			-190 ... 600
	biaxial drop weight (tension + tension by)					■	■				RT
fracture toughness K [ $Nmm^{-2/3} s^{-1}$ ]			■	■	■	■	■			-190 ... 400	
triaxial	gas gun – penetration simulator							■	■	■	RT
	flyer plate (IPCP Moscow)									■	-190 ... 600
	compression and hydrostatic compression (TU Chemnitz)	■	■	■	■		■				RT
	servohydraulic (tension, compr. + torsion + hydrost. compr.)	■	■	■	■						RT
	tension + tension + tension	■	■	■	■		■	■	■		-190 ... 600

FIG. 2. Testing capabilities needed for impact dynamic material characterization. Testing facilities in blue are available at Nordmetall GmbH.

the determination of the real material behavior. However, different special designed devices for certain applications of dynamic testing of materials exist, e.g. Hopkinson bars for compression and tensile testing, rotating wheels for tensile loading or drop weight towers for compression or flexure loading.

For modeling of the constitutive behavior of materials, uniaxial data are mostly sufficient for the application of simple phenomenological equations and for the description of flow stress and strain hardening behavior (e.g. [1, 2]). If failure is going to be considered, uniaxial experiments are not sufficient for characterization of the material behavior. Both the flow stress and failure are significantly influenced by strain, strain rate and temperature. Therefore, the material must be investigated using a broad range of loading conditions. In addition, compared to flow stress behavior, failure is largely influenced by stress state (especially by stress triaxiality). Hence, multiaxial testing by using stress concentrators like notches (Charpy impact test) or cracks (fracture toughness) are necessary. Additionally, complex and defined stress states, e.g. those observed during forming processes, have to be considered using combined loading states, e.g. multiaxial tensile testing superimposed by hydrostatic pressure, whereby all the tests have to be performed at high loading rates (Fig. 2).

Additionally, most of the materials studied under impact dynamic loading are not loaded monoaxially in later use. Most applications are characterized by

a complex geometry which normally leads to a complex loading state showing stress concentrations and high stress triaxialities. To investigate the impact component behavior, high quality dynamic measurement data (especially for force and deformation measurements) is required. Additionally, a large amount of impact energy is needed for the dynamic deformation of components. This has led to the design and development of new testing facilities which are capable of meeting the new demands of dynamic component testing.

The following sections demonstrate how special emphasis is put on high strain, high strain rate and high temperature testing, using high speed torsion loading and multiaxial material and component testing using high energy mechanical testing devices for tensile and compression/flexure loading.

### 3. HIGH SPEED TORSION TESTING

The parameter identification of constitutive equations used nowadays in finite element analysis of forming or cutting processes, are mostly based on monoaxial experimental data from high rate and in some cases high temperature compression or tensile tests. Thereby, the strain reached in tensile or compressive deformation of materials is limited and does not match real forming or cutting process, where plastic strains larger than  $\varphi = 2$  or  $3$  can be observed (e.g. [3, 4]). Especially the stress softening behavior due to recrystallization processes during deformation cannot be measured by compression or tensile tests.

Using torsion loading, this mismatch can be overcome, because no geometrical instability or friction effects lead to limited plastic deformation of the material, only the deformation capability of the material itself. Performing torsion tests to reach high plastic strains is familiar in material testing and characterization. To ensure a good predictability of material behavior in real engineering processes like rolling or turning, the material behavior has to be known at high strain rates and high temperatures. To solve this challenge, a new universal torsion testing machine was designed in cooperation between the Nordmetall GmbH and Chemnitz University of Technology (Fig. 3). The machine can be used for quasistatic tests by means of an electrical drive for loading the specimens, as well as for impact dynamic tests using an integrated flywheel construction.

For quasistatic tests, the specimens are fixed at both ends. Using a high power electrical drive, the specimen is loaded until failure of the material occurs. The torque during deformation is measured using a calibrated and adjusted load cell. The deformation is measured either by strain gages applied directly to the specimen and/or by an incremental gage of the machine. Dynamically, the force measurement is based on the principles of one-dimensional wave propagation effect and the Hopkinson principle. Thereby, the specimen is fixed directly on the Hopkinson bar containing strain gages. The lower end of the specimen

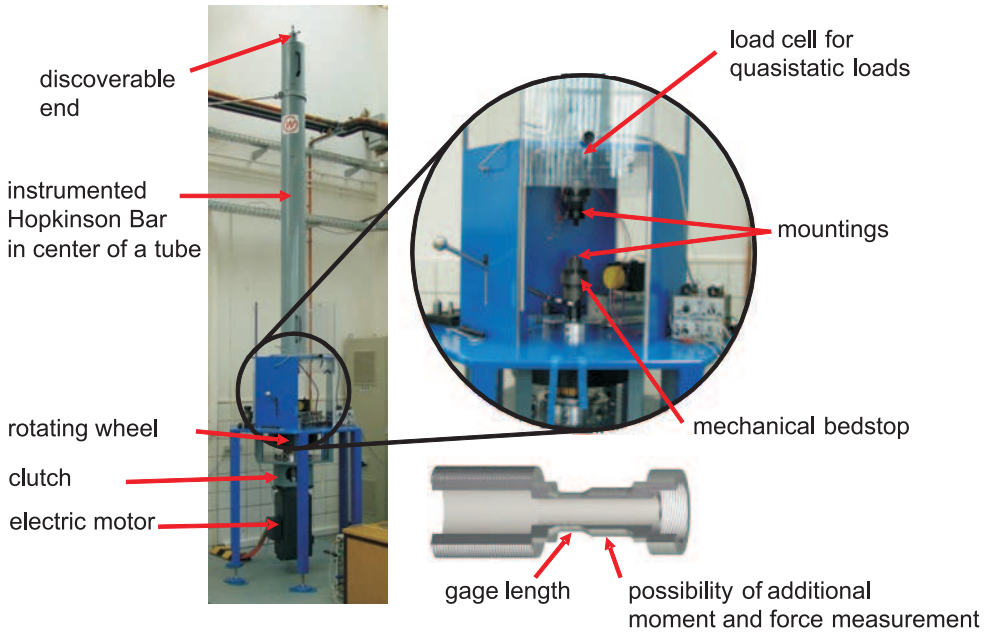


FIG. 3. Combined static and impact dynamic universal testing machine.

remains free. To ensure an impact loading of the specimen, a rotating wheel is accelerated by an electrical drive until a desired velocity is reached. Using a specially designed clutch device, the rotation is launched to the lower end of the specimen and the material is loaded by an impact torsion load. Due to the high mass of the flywheel and its rotation, the stored energy is sufficient to deform the specimen until fracture. Thereby, shear rates of approximately  $200 \text{ s}^{-1}$  can be reached, whereby a high signal quality of the load measurement can be assured. For both experimental setups, an inductive heating system can be integrated into the process, and high temperature investigations up to  $1300^\circ\text{C}$  can be performed. Hence, high strain, high strain rate, and high temperature data, leading to material behavior matching real cutting or forming processes, can be obtained.

In Fig. 4, an example for the behavior of a low alloyed steel at high strain rate and high temperature torsion loading is shown. It can be seen that the plastic deformability of the material is increased significantly from  $\varphi = 2$  at  $800^\circ\text{C}$  to  $\varphi = 10$  at  $1200^\circ\text{C}$ . From the experimental data, the transition from elastic to elastic-plastic behavior as well as strain hardening behavior can be evaluated. One of the great advantages of the torsion test is shown in Fig. 4. After reaching a stress maximum, the onset of recrystallization in conjunction with decreasing measured flow stresses can be found. This demonstrates that the onset of softening is strongly dependent on strain, strain rate and temperature.

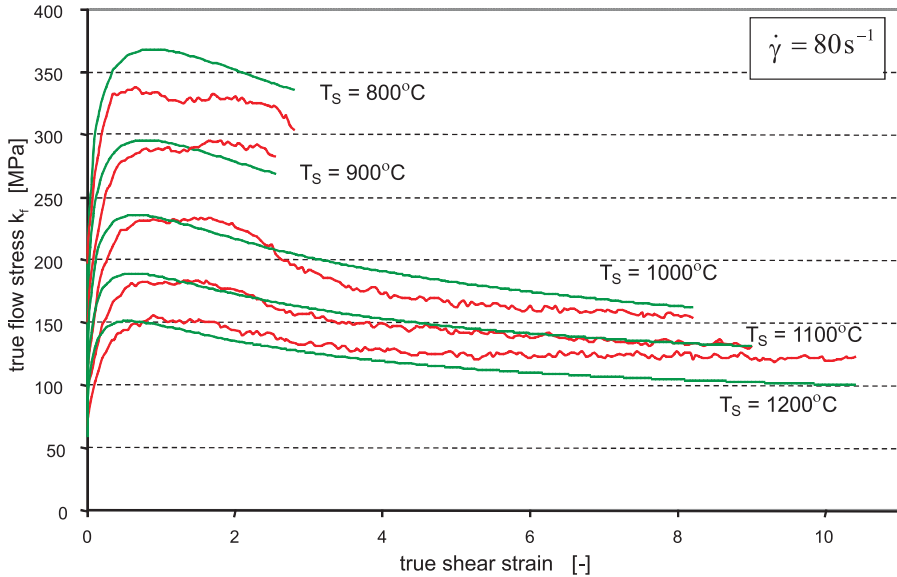


FIG. 4. Flow stress evolution of a low alloyed steel at high strains, high shear rate and high temperatures: comparison of experimental data and modeled data using the Hensel-Spittel approach [5].

Additionally, from Fig. 4 a comparison between experimental measured and modeled data, using Hensel-Spittel [5] (Eq. (3.1)) approach, can be evaluated as described in their publication.

$$(3.1) \quad k_f = A \cdot e^{m_1 T} \cdot T \cdot \varphi^{m_2} \cdot e^{m_4/\varphi} \cdot (1 + \varphi)^{m_5 T} \cdot e^{m_7 \varphi} \cdot \dot{\varphi}^{m_8} \dot{\varphi}^{m_8 T}.$$

It can be seen that experimental and modeled data show a good agreement over the whole range of plastic strains and temperatures. Even the flow stress decrease due to recrystallisation processes can be predicted using the Hensel-Spittel approach. Based on these data, a good prediction of the process behavior e.g. in rolling processes using finite element analysis, can be expected. It should be emphasised, that most of the common constitutive equations used in finite element simulations, like Johnson-Cook or Zerilli-Armstrong, cannot predict dynamic recrystallisation phenomena. Hence, not only experimental data are required, what matches real process behavior, but also equations used for the constitutive description of the material behavior under such conditions must fulfill these requirements.

#### 4. HIGH SPEED MULTIAXIAL TESTING

Until now only monoaxial material behavior of a virgin material was investigated and discussed. In real engineering applications usually multiaxial loading

occurs. Additionally, materials used in technical products and components normally pass through a variety of different manufacturing steps including forming, as well as cutting and joining technologies. Furthermore, the material or component behavior might be changed during its life cycle use. This may be caused by alteration or fatigue processes, especially in automotive and automobile industry, processes like welding or glueing play a key role in manufacturing today's innovative products. However, less is known about the dynamic behavior of components under a multiaxial dynamic loading.

A new experimental test setup was designed and built at Nordmetall GmbH ([www.nordmetall.net](http://www.nordmetall.net)) to investigate the material behavior under a multiaxial dynamic loading condition, and to include the influence of manufacturing history (welding etc.) and pre-damaging, due to fatigue in life cycle use compared to virgin material properties. Special focus is laid on a critical biaxial tensile-tensile stress state, which might occur for example under blast loading of structures and vehicles, or even under crash conditions. Normally, component testing under such conditions for automotive applications is performed at high impact velocities (10–20 m/s) that are obtained by a drop weight device having large drop heights. Thereby, high quality force-time measurements during deformation can not be obtained. This is because the large ringing of the signals that are superimposed on the output signal cannot be filtered out. Therefore, we enhanced the weight and reduced the drop height and the impact velocity and get undisturbed signals. The falling weight of 5 t provides sufficient energy during the test to deform most of the components to fracture.

The test setup used for dynamic biaxial tensile-tensile loading of steel plates is shown in Fig. 5. The plate is fixed on the top of a steel tube and impacted by a semi-spherical punch on the top site. During deformation, the deflection is measured by an incremental gage. The force-time characteristic is measured directly on the punch. A high-speed deformation field measuring system technique was applied in order to measure the real deformation behavior of the steel plate during impact loading. Thereby, the three-dimensional local deformation field at the bottom of the steel plate is measured during the entire process, from onset of plastic flow to fracture.

For the tests, three different states of the steel plates (plain, pre-notched and cracked, welded stringer) of the same thicknesses and two different materials were used. The results of the dynamic biaxial tensile-tensile tests are summarized in Fig. 6 and Fig. 7.

Shown in Fig. 6 are the recovered, biaxially loaded specimens. For both materials, no failure was observed for the plain steel plate. All the energy provided by the falling weight was absorbed by the material as plastic deformation. If the material is pre-damaged, either by a mechanical or a metallurgical notch (1 mm deep fatigue crack or welded stringer), both materials fail during biaxial

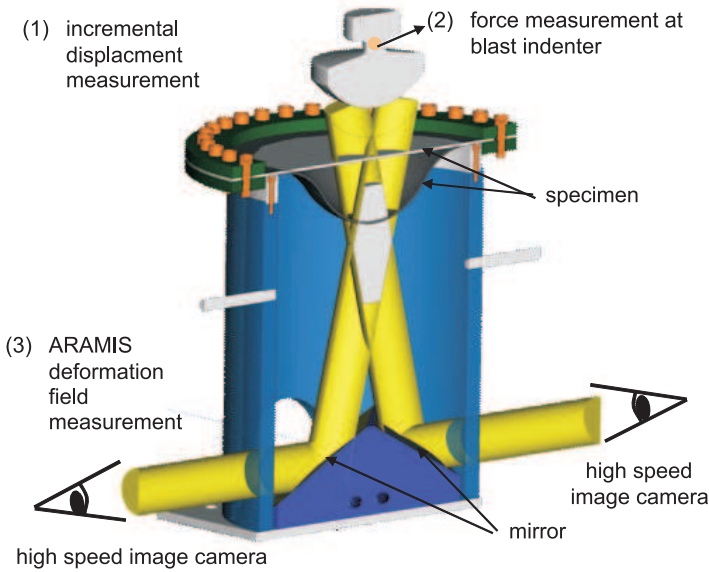


FIG. 5. Experimental test setup for high speed biaxial tensile-tensile-tests of steel plates, including high speed deformation field measuring system.

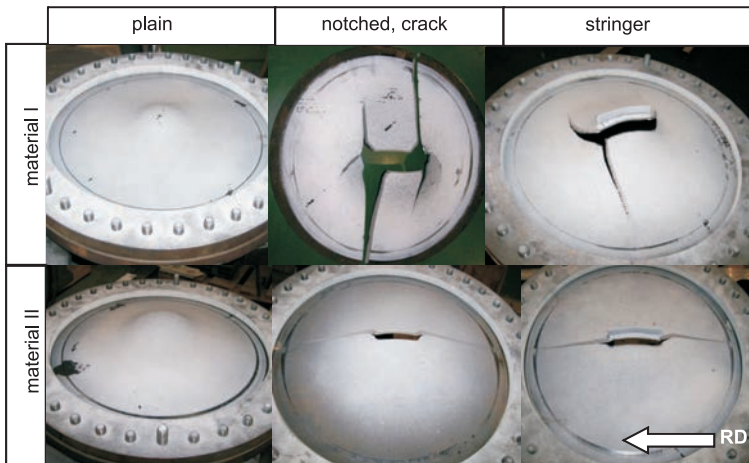


FIG. 6. Failure characteristics for two different materials at different pre-treatment states after biaxial testing.

tensile-tensile loading. For material II, a straight crack propagated through the whole specimen, whereas for material I branching occurred during crack propagation. If the measured force-time signals are compared (Fig. 7), one finds the highest strength for material I, if the material is tested in this virgin state (plain

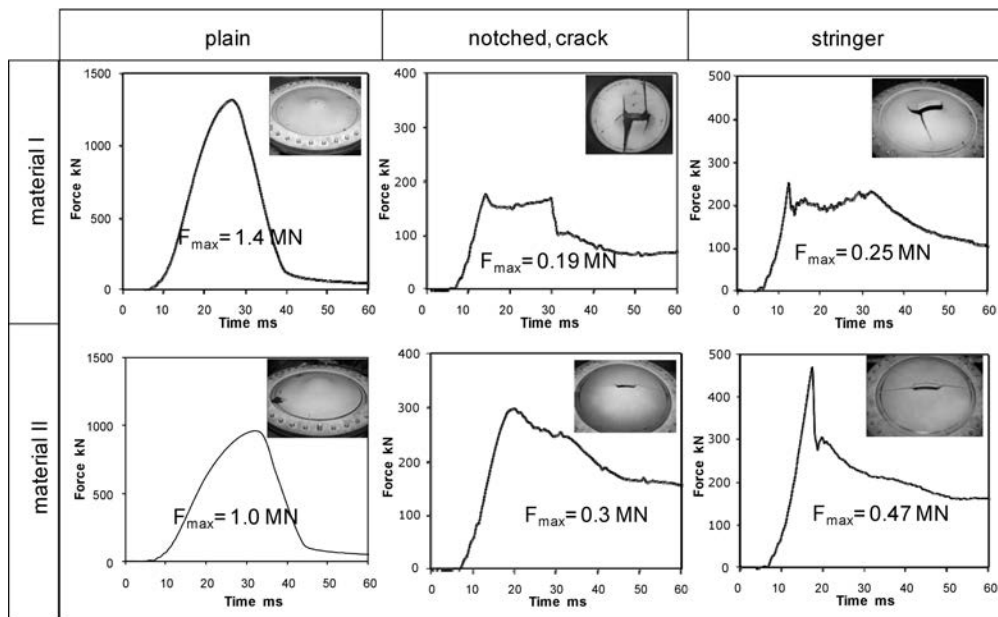


FIG. 7. Force-time behavior of two different materials with different stress-states at dynamic biaxial loading.

condition). If pre-damaging of material I occurs, the measured maximum forces are decreased dramatically. Only a sixth to a seventh of the initial maximum load can be sustained until the material fails. For material II, a similar decrease of the maximum load was observed. However, although material II is weaker in plain condition, it can be observed that the smaller influence of mechanical or metallurgical notches of material II leads to a better performance compared to material I.

Until now, material behavior is mostly considered in its virgin and undamaged condition. To ensure a high level of reliability and safety of engineering products and systems, the influence of manufacturing processes and their influence on the final mechanical properties of engineering materials have to be considered as well.

## 5. HIGH SPEED TENSILE TESTING USING A FLYWHEEL WITH A HIGH STORED ENERGY

Based on the experience obtained from drop weight tests with high stored energy, the principle was transferred to a new flywheel device. This rotating wheel with a comparably low velocity, but a high stored energy due to a 10 t mass flywheel, can impact specimen with a maximum velocity of 12 m/s.

This new innovative testing machine at Nordmetall GmbH enables dynamic investigations of large engineering components, ensuring that a high quality measurement of the force-time signal is obtained. A schematic picture of the machine is shown in Fig. 8. The functionality follows the principles of commonly known rotating wheel devices (e.g. [6]), but provides a high amount of energy for the dynamic deformation of high strength and/or high deformable and/or large parts and specimens. Hence, a new quality of material and component input data for finite element analysis, as well as for the experimental verification of numerical results, can be expected.

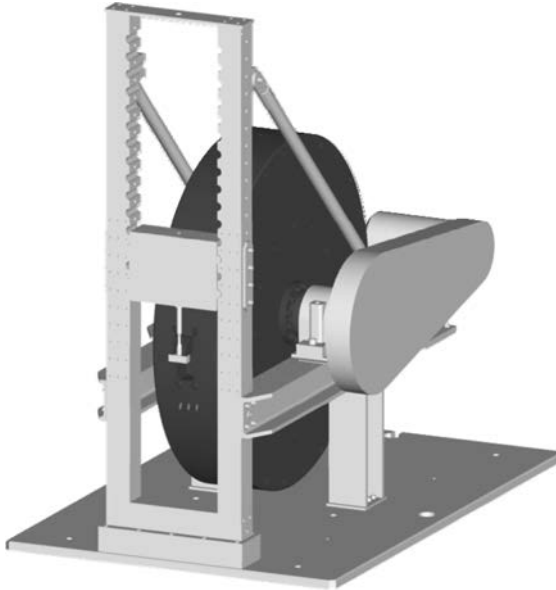


FIG. 8. Rotating wheel device of Nordmetall GmbH with a high amount of stored energy, by a 10 t flywheel ( $\varnothing 2$  m) for dynamic component testing of engineering materials.

## 6. CONCLUSIONS

This paper contains a short overview about different testing facilities and the material behavior, including monoaxial and multiaxial testing under high rate loading. Specifically the overview concerns discussions of difficult loading conditions and loading states such as high temperature and high strain loading ( $T > 1200^{\circ}\text{C}$ ,  $\varphi > 1$ ) and multiaxial impact tests. Special emphasis was laid on the influence of the manufacturing history of a material, on the dynamic properties under biaxial tensile-tensile loading. A dramatic decrease of the deformability and loading capacity was observed, if the material being tested contains a pre-damaged state by a metallurgical or mechanical notch.

## REFERENCES

1. G. R. JOHNSON, W. H. COOK, *A constitutive model and data for metals subjected to large strains, large strain rates and high temperatures*, Proc. of the 7th International Symposium on Ballistics, The Hague, 541–547, 1983.
2. F. J. ZERILLI, R. W. ARMSTRONG, *Dislocation-mechanics-based constitutive relations for material dynamics*, Journal of Applied Physics, **61**, 5, 1816–1825, 1987.
3. T. HALLE, L. W. MEYER, *Influence of different material models on the result of numerical high speed cutting simulations*, [in] Proc. of the 1st International Conference on High Speed Forming, Kleiner [Ed.], Dortmund, 133–142, 2004.
4. L. W. MEYER, C. KUPRIN, T. HALLE, *High rate material behavior at hot forming conditions*, Mechanics of Time-Dependent Materials, **13**, 1, 49–62, 2009.
5. M. SPITTEL, S. NEUBAUER, *Betrachtungen zur mathematischen Fließkurvenmodellierung*, Neue Hütte, **28**, 1, 21–25, 1983.
6. L. W. MEYER, *Werkstoffverhalten hochfester Stähle unter einsinnig dynamischer Belastung*, Ph.D. Thesis, Dortmund University of Technology, 1982.

## RESEARCH ON INFLUENCE OF IMPACT OF MICROPARTICLES AND SEWING NEEDLES ON DESTRUCTION OF SOLID BODIES

B. D. K h r i s t o f o r o v

**Institute of Geosphere Dynamics  
Russian Academy of Sciences**

38 building 6, Leninsky prospect, Moscow, 119334, Russian Federation  
e-mail: khrist@idg.chph.ras.ru

Impact of powders and sewing needles accelerated by explosion on various obstacles has been studied. Formation of channels up to 100 particle diameters in length has been observed when corundum and tungsten powders impacts on steel and duralumin at speeds up to 2 km/s. A mechanism of such super deep penetration of powder jets into metals has been proposed. The possibility of destroying by needles such objects as plexiglass blocks, antimeteorite screens, containers with elastic and explosive materials with a released energy exceeding the energy of needles has been shown. At impact speeds up to 400 m/s the depth of needles penetration into metals is 3–5 times higher than the one calculated for pointed rods at plastic work. The obtained results can be useful for modeling of impact of meteorites, space scraps and technological wastes on space aircrafts and their components.

**Key words:** impact, microparticles, needles, obstacles, penetration, destruction, modeling, striker.

### 1. INTRODUCTION

Conducting of space research is complicated recently by growth of cosmic dust and debris. Modeling of their impact on space equipment is usually carried out at speeds close to the cosmic ones for spherical strikers under conditions of both melting and evaporation of the substances. The depth of penetration does not exceed several diameters for spherical strikers and weakly depends on the properties of colliding materials [1, 2].

Super deep penetration into targets by powders at speeds up to 3 km/s was considered in [3]. In accordance with the mechanism of super deep penetration proposed in [4], the plastic flow of metal does not arise at a high strain rate, and under brittle fractures particles penetrate into cracks for big depths with lower energy losses than at plastic flow.

Presented are the results of a study of impact of powders and sewing needles on obstacles at speeds ranging from 0.1 to 2 km/s when melting and evaporation have a low effect on penetration. Special attention is paid to the probability and

mechanism of realization of super deep penetration of powders and needles into targets. The results can be useful for modeling of impact of meteorites, space scraps and technological wastes on space aircrafts and their components [5, 6].

## 2. EXPERIMENTAL ARRANGEMENT

Targets made of steel, duralumin, aluminum, titanium, plexiglas, aluminum containers with plexiglas, pressed salt, gunpowder and various explosive substances were used in the experiments. Powders of both corundum ( $\text{Al}_2\text{O}_3$ ) and tungsten with the particle diameters up to 50 microns, sewing needles with the Krupp hardness more than  $600 \text{ kg/mm}^2$ , weights of 0.2–1.3 g, diameters  $d = 0.9$ –2.2 mm, lengths  $l = (30\text{--}50)d$ , and wires made of copper and annealed steel were used as strikers. Strikers were accelerated up to the speeds of 0.5–2 km/s by explosive charges with 60 mm diameter and weights up to 200 g. Some needles were accelerated to the speeds of 0.15–0.6 km/s in an explosive shock tube with the mass of the explosives up to 5 g. The velocity  $U_0$ , impact energy  $e$ , depth of penetration in the obstacle  $L$ , volume of the holes  $V$  and kinematics of the needle motion were measured using the electric contact method and a high-speed movie camera with external illumination.

## 3. MEASUREMENTS

After impact of powders on metals, erosion of the target surface and appearance of deep channels on their cross section were observed. The photographs show the emergence of powder jets accelerated by the explosion. Figure 1 shows a typical photo (microsection after etching, increased 200 times) of duralumin D16 after an impact of corundum powder with a particle diameter up to 50 mi-



FIG. 1. Photo of duralumin D16 after an impact of corundum powder at the speed of 1.5 km/s.

crons and the speed of 1.5 km/s. The channel length of about 50 powder particle diameters is more than an order of magnitude larger than typical channel lengths for high velocity strikes [1, 2]. The number of channels increases with the thickness of powder. Channels have not been observed at impact velocities  $U_0 \geq 2$  km/s.

Some results of measurements and calculations of collisions of needles with metals are shown in Table 1 and following figures, where  $h$  is the thickness of impactor;  $m$ ,  $d$ ,  $e = mU_0^2/2$  are the mass, maximum diameter, and kinetic energy of the needle;  $L$ ,  $\Delta L$  are the length of the hole and the height of the needle tip over the hole in the target;  $V$  is the volume of the hole ( $P^* = e/V$  in the experiments when needles do not breach the target),  $H_1$  is the dynamic hardness of the material (which does not depend on speed),  $H_2$  is the Brinell hardness, and  $\tau$  is the shear strength [1, 5].

**Table 1.**

tests			needles				measurements				calculations	
No.	$U_0$ [m/s]	$h$ [mm]	No.	$m$ [g]	$d$ [mm]	$e$ [J]	$L$ [mm]	$\Delta L$ [mm]	$V$ [mm <sup>3</sup> ]	$P^*$ [GPa]	$V_c$ [mm <sup>3</sup> ]	$L_c$ [mm]
Steel-3, $H_k = 1.88$ GPa, $P_1^* = 2.9$ GPa, $\tau = 0.25$ GPa												
28	190	11.5	10	0.36	1.16	6.5	11	0	7.47	0.88	2.2	3.6
29	190	5.75	10	0.36	1.16	6.5	5.75	8				
38	190	5.75	10	0.36	1.16	6.5	5.75	8				
38a	190	5.75	12	1.3	1.6	23.4	5.75	60				
41	233	5.75	10	0.36	1.16	9.8	5.75	10				
41a	233	5.75	13	1.3	2.24	35.2	5.75	60				
Titan, $H_k = 2.14$ GPa, $P_1^* = 2.9$ GPa, $\tau = 0.32$ GPa												
64	280	14.5	13	1.3	2.24	50.96	12	0	20.3	2.5	16.1	10.2
65	320	14.5	13	1.3	2.24	66.6	14.5	0	28.4	2.35	21.0	12.1
67	350	14.5	13	1.3	2.24	79.6	14.5	3	28.4	2.8	25.3	13.3
69	420	14.5	13	1.3	2.24	115	14.5	10.5				
70	430	14.5	13	1.3	2.24	120	14.5	18				

Photos on Fig. 2 show the results of impacts of needles on targets of duralumin, steel, and plexiglas. When hardened needles breach metals channels with the diameter equal to the diameter of the needles are formed. Needles with the energy of 2 J breach 8 mm of duralumin or 16 mm of aluminum, whereas needles with the impact energy of about 6 J breach more than 11 mm of steel, 12 mm of duralumin or 20 mm of aluminum, respectively. The minimal specific energies  $e/V$  for channel formation are 0.2, 0.5, 1, and 2 kJ/cm<sup>3</sup> for aluminum,

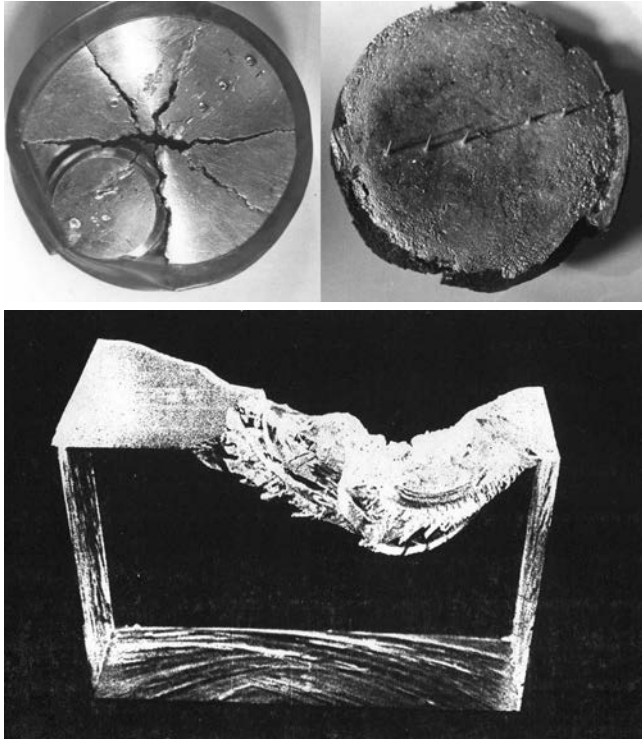


FIG. 2. Results of the impact of needles on the targets of duralumin, steel, and plexiglas.

D16T, steel, and titanium, respectively. Simultaneous impact of needles along the diameter of the circle of a target causes its disintegration along these lines.

During the impact of needles No. 13 with the energy 96 J each on a plexiglas block sized  $10 \times 7 \times 5 \text{ cm}^3$  a piece of the  $50 \text{ cm}^3$  size was thrown out because the stored elastic energy was released when cracks came out to the surface. A model of an antimeteorite screen consisting of three 1 mm thick duralumin plates with 3 mm gaps in between and an additional 12 or 14.5 mm thick duralumin plate positioned behind it were breached through by needles No. 13 at the speeds of 350 and 430 m/s respectively. Containers with plexiglas and salt impacted by needles were destroyed or plastically deformed due to allocation of the stored elastic energy of the samples  $e = \sigma^2 V / 2E$  from their brittle fracture. The elastic compression  $\sigma$  was previously created on the ends of the container by bolt clamped plates. Allocation of energy occurs along the axis of an impact, apparently because the stored elastic energy cumulates there. Containers with gunpowder, pressed PETN, and RDX were destroyed because of burning of the samples upon an impact with needles which penetrated through the walls of the container. Containers with plastic explosives were breached by needles without significant external effects.

## 4. DISCUSSION OF THE RESULTS

In the tests with powders at the impact velocities of  $U_0 \leq 2$  km/s, smaller than the speed of cracks in metals, conditions of a super deep penetration, when the length of the channels exceeded a hundred as much the particle diameters, sometimes were encountered. It was assumed that this was accompanied by brittle fracture under the action of powder jets when the particles penetrated into a crack, one after another. Although for microparticles the probability of a super deep penetration is small, this effect should be taken into account for their long-term interference with space objects.

Penetration of pointed rods into a hard material was studied in [1, 2, 7]. In a simplest formulation the following equation of motion is solved when a rod makes plastic work against the force  $SP^*$ :

$$(4.1) \quad mUdU/dx = -SP^*,$$

where  $S(x)$  is the section of the rod. Resistance to penetration  $P^* = P_1^* = H_1 + H_2 = \text{const}$  at  $U_0 \leq 2\text{--}3$  km/s, where the dynamic hardness  $H_1$  of the material does not depend on velocity and  $H_2$  is the Brinell hardness, was studied in [5]. Calculation of  $P_1^*$  at these values gives a penetration depth  $L$  3–5 times smaller than in the tests with needles at the impact velocities of 150–300 m/s. Therefore, it was suggested that at these impact velocities work of brittle fracture and friction is defining, plastic flow has no time to develop, and the plastic work is lower than the calculated one.

Figure 3 shows the dependence of the penetration resistance  $P^* = e/V$  on the impact velocity  $U_0$  of needles with different sizes. Figure 4 shows the

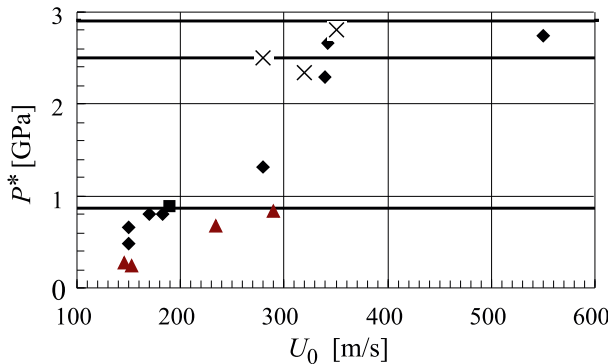


FIG. 3. Dependence of the resistance  $P^*$  to penetration of needles on the impact velocity  $U_0$ .

Squares, triangles, rhombi, and crosses are used for steel, aluminum, duralumin, and titanium, respectively. For comparison, the parallel lines are the values  $P_1^* = H_k + H_b$  for plastic work [2, 7], which equal to 2.9, 2.5, and 0.86 GPa for pointed rods of steel, duralumin, and aluminum, respectively.

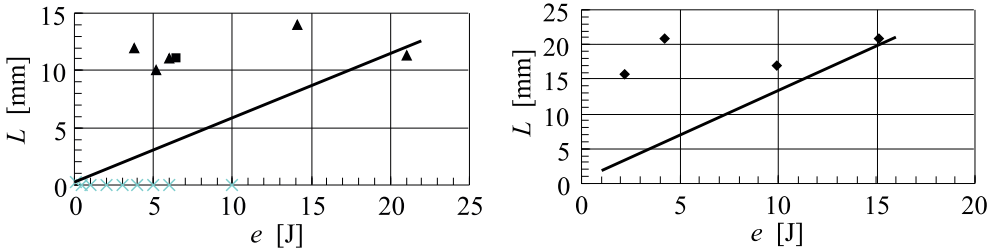


FIG. 4. Dependence of the penetration depth  $L$  on the impact energy  $e$  of needles No. 10 for steel and duralumin as targets (on the left) and of needles No. 7 and 10 for aluminum as a target (on the right). The meaning of symbols is as in Fig. 3. Solid lines denote calculations for plastic work at  $P_1^* = 2.5$  and  $0.86$  GPa for duralumin and aluminum respectively.

dependence of the penetration depth  $L$  on the impact energy  $\varepsilon$ . When  $U_0 \approx 150$ – $300$  m/s, values of  $P^*$  are several times smaller (and the depths of penetration are respectively higher) than for rods [3]. With the increase of the impact velocity values up to  $400$ – $500$  m/s, the value of  $P^*$  stops increasing and approaches the values of  $P_1^*$  in [3], which characterize the plastic work.

Figure 5 shows the dependence of  $V(e)$  on the investigated materials. The reduction of the kinetic energy of a needle (which determines its penetration) when the plastic losses are small was estimated. The resistance to penetration  $P^*$  of hard rods into elastic-plastic materials was shown in [7]:

$$(4.2) \quad P^* = \tau + 2\gamma l/S, \quad \gamma = \gamma_0 + \gamma_1 = K^2/2E,$$

where  $\tau$  ( $\approx 0.2$  GPa for steel) is the shear strength of the target material;  $\gamma$  is the surface energy of cracks appearance per unit of length  $l$ ;  $S$  is the area of contact of a rod with the surface of a crack;  $\gamma_0$  is the energy breaking of cracks;  $\gamma_1$  is the energy of plastic deformation of a crack;  $K$  is the parameter of a crack which according to the static experiments is equal to  $200$  kg/mm $^{3/2}$  for steel and  $1.7$  kg/mm $^{3/2}$  for glass; and  $E$  is the Young's modulus. When  $\gamma_0 \ll \gamma_1$  (for steel

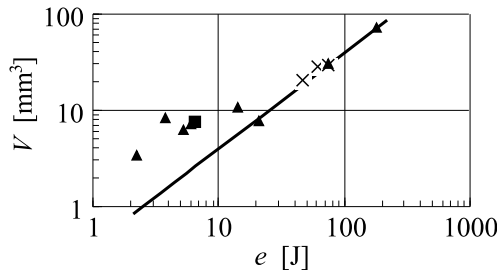


FIG. 5. Dependence of the channel volume  $V$  on the needle energy  $e$  for different materials. The meaning of symbols is as in Fig. 3. The curve denotes the calculations for plastic work at  $P_1^* = 2.5$  GPa for duralumin.

$\gamma_0 \approx 1$  N/m and  $\gamma_1 \approx 10^4$  N/m) the surface energy of cracks  $\gamma = \gamma_0 + \gamma_1 \approx \gamma_1$  is determined by the plastic work.

At the characteristic for the experiments strain rates  $d\varepsilon/dt = U/d \approx 10^6$ – $10^7$  s<sup>-1</sup>, apparently, the condition  $\gamma_1 \ll \gamma_0$  is realized, i.e. plastic deformation has no time to develop. In this case  $\gamma \approx \gamma_0$ , which strongly reduces the resistance to deformation upon a little friction, for example, due to melting of the material. With a reduction of the needle diameter  $d$ , the velocity of deformation increases and the conditions of brittle fracture can be satisfied at lower speeds of impact. This calculation explains qualitatively the test results, where the possibility of destruction of large constructions with the minimal impact energy was shown. At the impact velocities above 300–400 m/s resistance to penetration of the needle  $P^* \approx P_1^*$  causes their transverse vibrations and the loss of their stability. Needle penetration depths are consistent with those obtained for pointed rods [2, 7].

## 5. CONCLUSION

Impact of corundum and tungsten powders and sewing needles on various barriers was studied at the velocities of 0.1–2.5 km/s when melting and evaporation has little effect on penetration. It was observed that powders at the speeds of up to 2 km/s and sewing needles at the speed of 0.6 km/s penetrate into metals on depths over 100 and 50 impactors' diameters respectively. Formation of powder jets was noted when powder was accelerated by blasts. A mechanism of such a super deep penetration of powder jets into metals was proposed, i.e. brittle fractures occur with minimal losses of energy, therefore, plastic flows have no time to develop. An accurate estimation of the probability of a super deep penetration of powder is not possible. The possibility of destruction of various designs, e.g. blocks of plexiglas, antimeteorite screens, containers with elastic and explosive materials, was shown. This happens due to the release of the stored energy, which is much greater than the energy of the needles. The results can be useful in industry and nanotechnology for modeling of impact of meteorites, space scraps and technological wastes on space aircrafts and their components [5, 6].

## REFERENCES

1. N. A. ZLATIN, G. I. MISHIN, *Ballistic devices and their use in experimental studies*, Mir Publishers, Moscow, 344, 1974.
2. S. S. GRIGORYAN, *Dynamics of impact*, Mir Publishers, Moscow, 1985.
3. S. S. GRIGORYAN, *On the nature of super deep penetration of hard microparticles in hard materials*, Dokladi AN SSSR, **202**, 6, 1319–1323, 1987.

4. K. I. KOZOREZOV, V. I. MAKSIMENKO, S. M. USHIRENKO, *Selected problems of modern mechanics. Part 1*, Moscow State University, Moscow, 1981.
5. V. O. SOLOVIEV, B. D. KHRISTOFOROV, *Development of methods for simulation of high-power radiation on the walls of the reactor chamber pulsed nuclear energy devices*, Problems of Mechanic Engineering, Automation, 3, 56–61, 2008.
6. B. D. KHRISTOFOROV, *Experimental simulation of the impact of space dust and debris on aircraft and their components*, Cosmic Research, 3, 263–268, 2011.
7. K. A. ALEKSEEVSKII, *On the penetration of the rod in the barrier at high speed*, Fizika Gorenia i Vzryva, 2, 99–104, 1966.

MECHANICAL RESPONSE OF HPFRCC IN TENSION  
AND COMPRESSION AT HIGH STRAIN RATE  
AND HIGH TEMPERATURE

E. Cadoni<sup>1)</sup>, A.M. Bragov<sup>2)</sup>, A. Caverzan<sup>3)</sup>,  
M. di Prisco<sup>3)</sup>, A. Konstantinov<sup>2)</sup>, A. Lomunov<sup>2)</sup>

<sup>1)</sup> **University of Applied Sciences of Southern Switzerland**  
**DynaMat Laboratory**  
Switzerland

<sup>2)</sup> **State University of Nizhny Novgorod**  
**Research Institute of Mechanics**  
Russia

<sup>3)</sup> **Politecnico di Milano**  
**Department of Structural Engineering**  
Italy

The mechanical response of High Performance Fibre-Reinforced Cementitious Composite (HPFRCC) has been analyzed at high strain rates and high temperature. Two experimental devices have been used for compression and tension tests: the traditional Split Hopkinson Pressure Bar for compression and the JRC-Split Hopkinson Tension Bar for tension. The HPFRCC was thermally damaged at 3 temperatures (200°C, 400°C and 600°C) in order to analyze the dynamic behaviour of this material when explosions and fires took place in a tunnel. Results show that significant peak strength increases both in tension and in compression. The post-peak strength in tension depends on the thermal damage of the material. Its strain-rate sensitivity and thermal damage have been illustrated by means of a Dynamic Increase Factor. These results show that it is necessary to implement new expression of the DIF for the HPFRCC, therefore more and more accurate and experimental studies using Kolsky–Hopkinson Bar methods are needful.

## 1. INTRODUCTION

The mechanical response of concrete structures subjected to impact loading and high temperature, main load conditions present in explosions and fires in tunnel, cannot be ignored in the design, but they have to be predicted and controlled starting by investigation into proper material models for cementitious composites, including strain-rate effects and thermal damage. The mechanical behaviour of cementitious composites when they are subjected to extreme temperatures, impacts or blast has still many aspects open to investigation.

As a matter of fact, a scanty information provided so far by such special equipments as the Split Hopkinson Pressure Bar (SHPB) and Split Hopkinson Tension Bar (SHTB) for very high strain rates (as in explosions) shows significant increases in peak strength. However, dynamic peak strength is not sufficient to design a structure subjected to a dynamic load. Moreover, fibre cementitious composites are often used to improve the impact resistance, preventing scabbing and fragmentation problems, due to their ability in energy absorption, but the link between the dynamic energy and the static energy absorption, its strain-rate sensitivity and thermal damage influence are not clear as yet. The work described herein focuses on the behaviour of thermally damaged High Performance Fibre-Reinforced Cementitious Composites subjected to high strain-rate in tension and compression that is presented and compared with results obtained in a static range.

## 2. EXPERIMENTAL PROGRAM

Compression and tension loading tests were carried out on 20 mm high, cylindrical specimens with a 20 mm diameter (see Fig. 1). The specimens subjected to tension test were pre-notched (notch = 1.5 mm) in order to prevent multiple fractures.

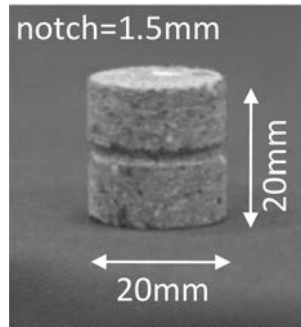


FIG. 1. Specimen for tension.

These specimens were tested under quasi-static conditions by a closed-loop electro-mechanical press and under high strain rates by a SHPB and a SHTB for compression and tension tests respectively.

### 2.1. Materials

The mix design of the HPFRCC material is specified in Table 1. Steel fibres are high carbon, straight fibres, 13 mm long, with a 0.16 mm diameter; their content is equal to 100 kg/m<sup>3</sup> [1].

**Table 1. HPFRCC Mix design.**

	Dosage (kg/m <sup>3</sup> )
Cement type I 52.5	600
Slag	500
Water	200
Super plasticizer	33 (l/m <sup>3</sup> )
Sand 0–2 mm	983
Fibres ( $l_f = 13$ mm; $d_f = 0.16$ mm)	100

Manufacturing process was composed by more phases. First of all, a 30 mm thick, 1.6 m wide and 0.60 m deep was cast in plane. The casting was carried out by applying a unidirectional flow in order to guarantee a certain fibre orientation. Twelve prismatic samples, 40 mm wide and 600 mm long, were sawn from the slab taking the larger side of beam samples parallel to the casting flow direction. Three specimens were tested in bending at room temperature [2–3]. Nine beam specimens, with the same geometry, were used to investigate the degradation of post-cracking residual strengths in bending after exposure to high temperatures [2–3]. From the bent specimens, several small cylinders, investigated here, were cored in the direction of tensile stresses to be tested in uniaxial tension at different loading rates. The thermal treatment of the samples was carried out in a furnace by performing thermal cycles up to three different maximum temperatures: 200, 400 and 600°C. A heating rate equal to 50°C/h was imposed up to the maximum thresholds, and then two hours of stabilization were guaranteed in order to assure a homogeneous temperature distribution within the sample volume. The temperature was then reduced with a rate of 25°C/h down to 100°C and then a cooling process at room temperature was carried out (see Fig. 2). For each cycle, three nominally identical samples were introduced into the furnace.

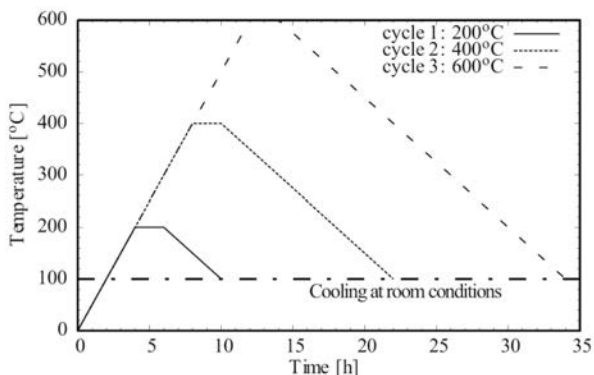


FIG. 2. Thermal cycles.

### 3. STATIC AND DYNAMIC TESTING SET-UPS

#### 3.1. *Quasi-static tension and compression tests*

In order to characterize the material behaviour in the static field, several uni-axial tension tests were carried out on notched cylinders with 20 mm diameter, and 20 mm height (notch depth = 1.5 mm), glued to the press platens by means of an epoxy resin. The tests were carried out by means of close-loop electro-mechanical press INSTRON 5867, in the laboratory of Politecnico di Milano – Polo Regionale di Lecco. The press has a maximum loading capacity equal to 30 kN. Two aluminium cylinders connected to the press by a knuckle joint were used as press platens. In both cylinders, a 5 mm deep cylindrical cavity with a 22 mm diameter was made in order to increase the glued sample surface. Stroke was considered as a feedback parameter during the tests. The displacement rate imposed during the tests was equal to  $5 \times 10^{-5}$  mm/s up to 1.5 mm and it was progressively increased up to  $10^{-3}$  mm/s. For each temperature (room conditions, 200°C, 400°C and 600°C), three samples were tested. The compression tests were carried out by means of an electro-mechanical press INSTRON 8562. The aluminium press platens were replaced by two steel platens. A thin layer of stearic acid was placed between samples and platens in order to reduce the friction.

#### 3.2. *Dynamic tension tests*

The dynamic direct tension tests were performed using a modified Hopkinson Bar called JRC-Split Hopkinson Tensile Bar (JRC-SHTB) [4–5], installed in the DynaMat laboratory of the University of Applied Sciences of Southern Switzerland (SUPSI) of Lugano (Fig. 3).

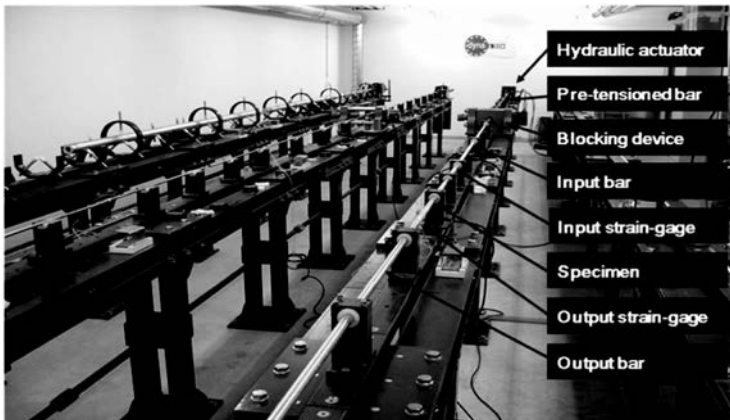


FIG. 3. Dynamic direct tensile testing set-up.

The JRC-SHTB consists of two circular aluminium bars, called input and output bars, having the lengths respectively of 3 m and 6 m, with a diameter of 20 mm, to which the HPFRCC specimen is glued using an bi-component epoxy resin. The input bar is connected with a high-strength steel pretension bar with a length of 6 m and a diameter of 12 mm. The pretension bar is used for the generation of the pulse loads. The hydraulic actuator placed at the end of the system is directly connected to one end of the pretension bar. The pretension bar is clamped at the other end by a blocking device. Pulling the pretension bar, the elastic energy is stored in it. Rupturing the fragile bolt in the blocking device, a tensile mechanical pulse of 2.4 ms duration is produced. It propagates along the input and output bars leading to fracture of the specimen.

The pulse propagates along the input bar with the elastic wave velocity  $C_0$ , during the propagation phase the wave shape remains constant. When the incident pulse ( $\varepsilon_I$ ) reaches the HPFRCC specimen, part of it ( $\varepsilon_R$ ) is reflected by the specimen whereas another part ( $\varepsilon_T$ ) passes through the specimen propagating into the output bar, as shown in Fig. 4. The relative amplitudes of the incident, reflected and transmitted pulses, depend on the mechanical properties of the specimen. Strain-gauges glued on the input and output bars of the device are used for the measurement of the elastic deformation (as a function of time), created on both half-bars by the incident/reflected and transmitted pulses, respectively. In Fig. 4 the raw signals measured on the input and out-

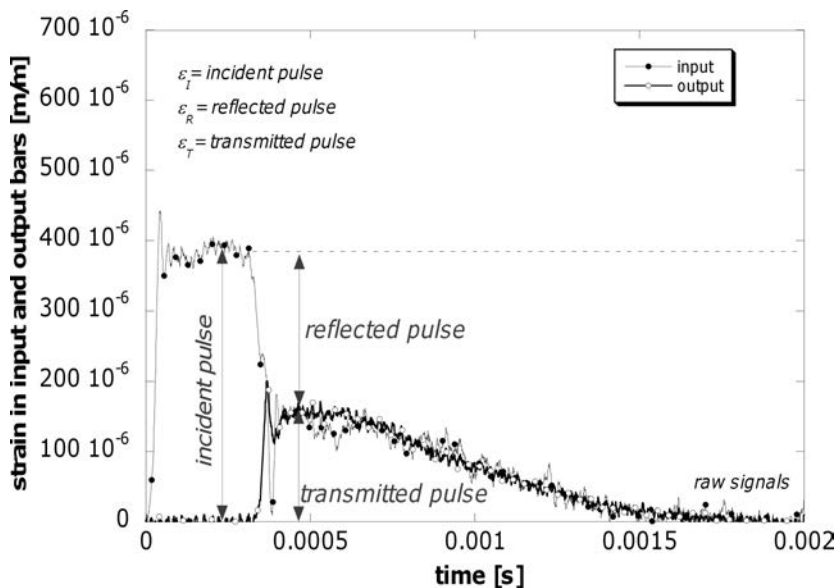


FIG. 4. Signals measured on the input and output bar versus time curves of HPFRCC.

put bars of the JRC-SHTB are shown. We can observe the clean resolution of incident, reflected and transmitted pulses, the sharp rise time of the incident pulse of the order of 30  $\mu\text{s}$ , and the nearby constant amplitude of the incident pulse. Moreover during the fracture process the specimen is subjected to the load equilibrium because the signals  $(\varepsilon_I + \varepsilon_R)$  and  $\varepsilon_T$  are equal.

By using the theory of the elastic wave propagation in bars, and the well substantiated assumption of specimen equilibrium attainment, the stress (Eq. (3.1)) and strain (Eq. (3.2)) as well as the displacement (Eq. (3.3)) and the strain-rate (Eq. (3.4)) in the specimen can be calculated [4–5]:

$$(3.1) \quad \sigma(t) = E_0 \frac{A_0}{A} \varepsilon_T(t),$$

$$(3.2) \quad \varepsilon(t) = -\frac{2 \cdot C_0}{L} \int_0^t \varepsilon_R(t) dt,$$

$$(3.3) \quad \delta(t) = -2 \cdot C_0 \int_0^t \varepsilon_R(t) dt,$$

$$(3.4) \quad \dot{\varepsilon}(t) = -\frac{2 \cdot C_0}{L} \varepsilon_R(t),$$

where  $E_0$  is the elastic modulus of the bars;  $A_0$  their cross-sectional area;  $A$  is the specimen cross-section area;  $L$  is the specimen gauge length;  $C_0$  is the sound velocity of the bar material;  $t$  is time.

### 3.3. Dynamic compression tests

The dynamic compression tests were performed using a Split Hopkinson Pressure Bar (SHPB), installed in the Dynamic Testing of Materials Laboratory of the Research Institute of Mechanics-Nizhny Novgorod University (Russia), which consists of an input (2) and an output (5) bar with the specimen (4) sandwiched between them, what is schematically shown in Fig. 5. When the strike bar (1) impacts onto the input bar, a compressive incident wave  $\varepsilon_I(t)$  travels along the input bar. Once it reaches the specimen, a reflected wave  $\varepsilon_R(t)$  and a transmitted wave  $\varepsilon_T(t)$  are generated, propagating along the input and output bar respectively. According to the one-dimension wave propagation theory, the forces and particle velocities/displacements at the two faces of specimen can be determined by those three waves recorded.

In Fig. 5a the Lagrangian graph describing the strain history of the two bars is also shown. In Fig. 6 the signals of the input and output of a dynamic

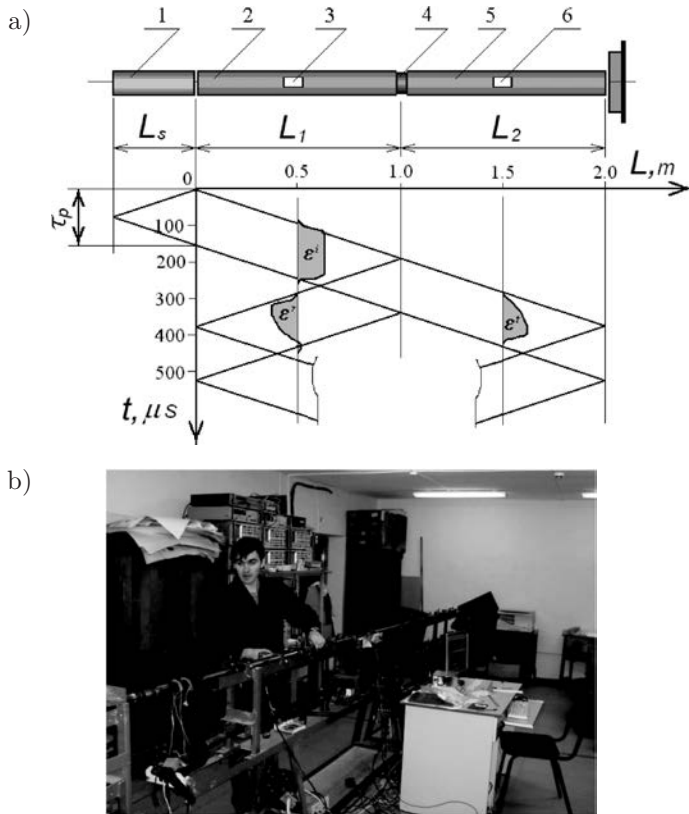


FIG. 5. Dynamic compression testing set-up: a) scheme and Lagrangian graph; b) view.

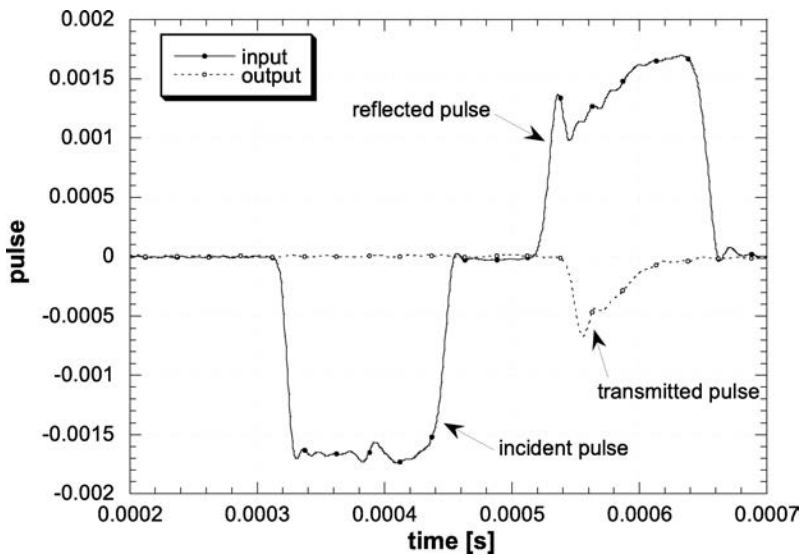


FIG. 6. Signals measured on the input and output bars versus time curves of HPRCC.

compression tests of HPFRCC specimen are shown. It can be observed that the failure of the specimen is reached just in the first loading cycle. By comparing Fig. 4 and Fig. 6 it can be noted that in the case of compression, the time necessary to bring the specimen at failure is about 100  $\mu\text{s}$ , while in the case of tension, more than 1.5 ms is needed.

#### 4. RESULTS AND DISCUSSION

The comparison between the tensile and compression behaviour at high strain rates of HPFRCC with different thermal damage is here presented. The tests were performed with a strain rate of 150  $\text{s}^{-1}$  in tension and 500  $\text{s}^{-1}$  in compression. The results are summarized in Table 2.

**Table 2. Dynamic results.**

Temperature [ $^{\circ}\text{C}$ ]	Compression strength [MPa]	$\text{DIF}_C$ (500 $\text{s}^{-1}$ )	Tensile strength [MPa]	$\text{DIF}_T$ (150 $\text{s}^{-1}$ )
20	117.4 $\pm$ 18	2.20	24.96 $\pm$ 2.3	2.85
200	162.0 $\pm$ 25	2.58	26.08 $\pm$ 1.0	2.61
400	134.4 $\pm$ 21	3.07	25.28 $\pm$ 3.9	2.27
600	132.0 $\pm$ 30	2.45	32.49 $\pm$ 1.5	5.40

High temperature exposure influences both the static and dynamic material behaviour. The comparison between static and dynamic tensile stress versus displacement curves are shown in Fig. 7. In order to highlight the first linear elastic branch and post peak behaviour close to the peak, a detail of the peak zones is plotted. Observing Fig. 7 it is possible to note that the behaviour changes as a function of the exposition to high temperature. As in a static tests, specimens cured at room conditions show a post-peak stress plateau up to a displacement of 0.4 mm. The constant stress plateau decreases with temperature growth. At 600 $^{\circ}\text{C}$  the behaviour is significantly changed, becoming weakly softening in the post-peak region. At this velocity, the peak increases with the exposition to high temperature as well as the post-peak strength decreases to disappear for higher temperatures.

By observing the fracture surface of the specimen it is evident as the failure type has changed (Fig. 7). In the first case (Fig. 7a), the observable hole in the specimen demonstrates the fibre pullout process occurrence, while in the second one (Fig. 7b) all the fibres are broken.

In Fig. 8 the stress versus displacement curves of the compression test, both in quasi-static and dynamic condition, are shown. The HPFRCC exhibits an increase of strength with increasing strain-rate, also in compression

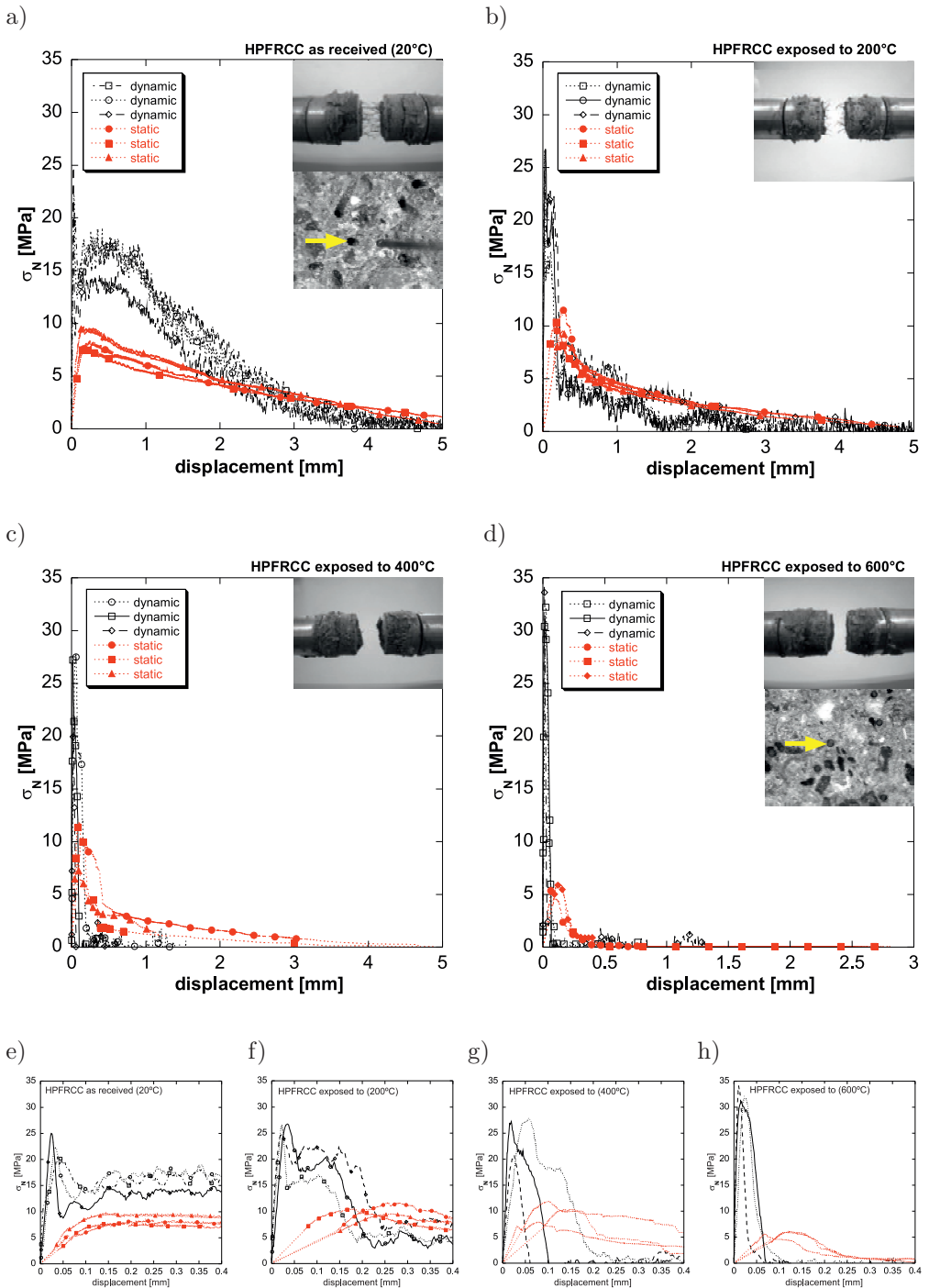


FIG. 7. Comparison of the tension quasi-static and dynamic stress vs. displacement curves of the tests at different temperature: a) 20°C; b) 200°C; c) 400°C; d) 600°C.

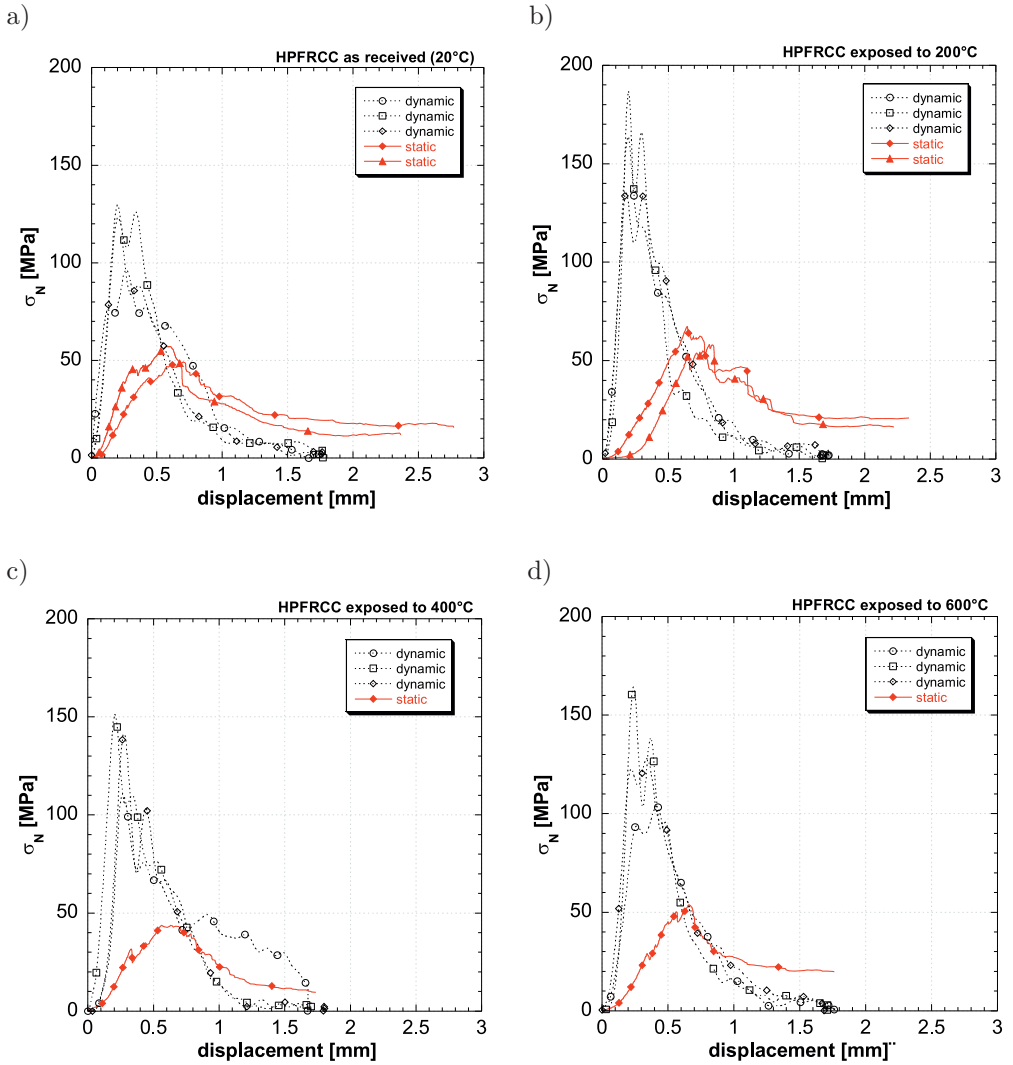


FIG. 8. Compression quasi-static and dynamic stress vs. displacement curves of the tests at different temperatures: a) 20°C; b) 200°C; c) 400°C; d) 600°C.

#### 4.1. Dynamic Increase Factor

Dynamic Increase Factor (DIF) has been extensively used in order to quantify the strain-rate effects for concrete, and some expressions of the DIF for the tensile and compression have been proposed. However, no expressions of DIF are available for HPFRCCs due to the lack of experimental results. Often these expressions are generated by experimental data obtained by different experimental

techniques, as the tensile strength obtained from direct or indirect tension tests (splitting, spalling, bending, etc.).

The most comprehensive model for predicting the strain-rate enhancement of concrete is presented by the CEB Model Code [6]. It provides specifications for the DIF for concrete in tension and compression.

The suggested expression are the following:

$$(4.1) \quad \text{DIF}_{\text{CEB,tension}} = \begin{cases} 1 & \dot{\epsilon}_d \leq \dot{\epsilon}_s, \\ \left(\frac{\dot{\epsilon}_d}{\dot{\epsilon}_s}\right)^{1.016\alpha} & \dot{\epsilon}_s < \dot{\epsilon}_d \leq 30 \text{ s}^{-1}, \\ \gamma \left(\frac{\dot{\epsilon}_d}{\dot{\epsilon}_s}\right)^{0.33} & \dot{\epsilon}_d > 30 \text{ s}^{-1}, \end{cases}$$

with  $\gamma = 10^{(7.11\alpha-2.33)}$ ;  $\alpha = 1/(10+6f_c/10)$ ;  $f_c$  is the static compressive strength in MPa, and  $\dot{\epsilon}_s = 3 \cdot 10^{-6} \text{ s}^{-1}$ .

$$(4.2) \quad \text{DIF}_{\text{CEB,compression}} = \begin{cases} 1 & \dot{\epsilon}_d \leq \dot{\epsilon}_s, \\ \left(\frac{\dot{\epsilon}_d}{\dot{\epsilon}_s}\right)^{1.026\alpha} & \dot{\epsilon}_s < \dot{\epsilon}_d \leq 30 \text{ s}^{-1}, \\ \mu \left(\frac{\dot{\epsilon}_d}{\dot{\epsilon}_s}\right)^{0.33} & \dot{\epsilon}_d > 30 \text{ s}^{-1}, \end{cases}$$

with  $\mu = 10^{(6.156\alpha-2)}$ ;  $\alpha = 1/(5+9f_c/10)$ ;  $f_c$  is the static compressive strength in MPa, and  $\dot{\epsilon}_s = 30 \cdot 10^{-6} \text{ s}^{-1}$ .

The prediction has been carried out by assuming a perfect uncoupling between thermal damage and strain effect, a compressive strength variable, with the temperature on the basis of performed experimental tests and a variation with high strain-rate according to CEB formulation. This prediction is indicated in Fig. 9 as ‘‘CEB’’ DIF: the comparison with experimental results is shown in Fig. 9.

The CEB formula overestimates the compression strength comparing those actually recorded in the tests for all four exposure temperatures. The overestimation may be due to the effect of fibres and their distribution. The analyzed material has fibres oriented in the direction of the load. As reported in [7] for the tension tests, increasing of the temperature the DIF does not significantly change up to the maximum temperature of 400°C, DIF is close to 2.5 till 400°C and suddenly goes up to 5.5 at 600°C. Looking at the results obtained in the compression tests, increasing of the temperature the DIF increase up to a maximum of 3 for 400°C, and slightly lower value than 2.5 for 600°C.

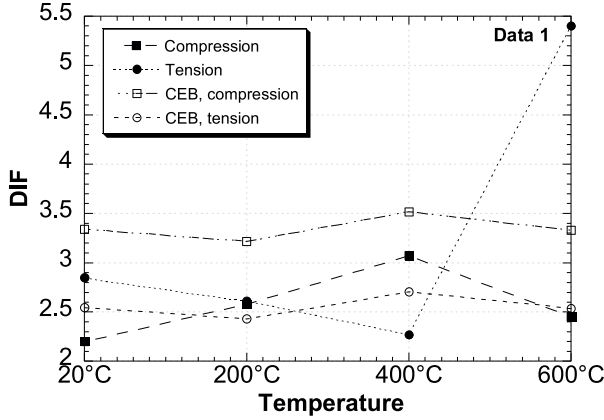


FIG. 9. Comparison between the experimental and CEB DIF at different temperature.

The CEB formulations were developed for concrete and its suboptimal estimate for other fibre-reinforced material; in a future paper, a new DIF formulation for HPFRCC will be proposed.

## 5. CONCLUDING REMARKS

The following remarks can be drawn from this study on the tension and compression behavior of HPFRCC under high strain-rates and high temperatures.

- The undamaged material showed a stress plateau in region close to the peak strength. This plateau was observed at different strain rates. Increasing the strain rate from  $10^{-6}$  to  $150 \text{ s}^{-1}$  the stress plateau grows from 8.5 to 15 MPa. This stress plateau seems to be rate-sensitive as well as the tensile strength.
- The material is strain hardening at room temperature in tension and under quasi-static loads; high temperature exposure up to  $400^\circ\text{C}$  does not decrease the tensile peak strength, slightly decreases the ductility before the single crack localization and progressively decreases the post-peak fracture energy; an abrupt peak strength decrease can be observed at  $600^\circ\text{C}$ .
- At high strain rate, the dynamic factor related to tensile peak strength is increased by high temperature exposure, passing from about 2.5 up to  $400^\circ\text{C}$  to more than 5 at  $600^\circ\text{C}$  at a strain rate of  $150 \text{ s}^{-1}$ .
- The compression strength increases with increasing the strain rate, obtaining at least two times the static value. This increase is influenced by the temperature.
- The dynamic compression strength could be influenced by the fibres, which are parallel to the load direction in the samples tested. New experimental

tests will be carried out on plain material in order to investigate the fibre influence.

#### ACKNOWLEDGMENT

The Authors are grateful to Matteo Dotta and Daniele Forni of the University of Applied Sciences of Southern Switzerland, Matteo Colombo and Giulio Zani of the Politecnico di Milano for their precious collaboration in the the laboratory tests. The research was partially financed by the project ACCIDENT ID 7629770 in the frame of INTERREG IT/CH 2006-2013 program.

Moreover a special acknowledgements goes to the Scientific & Technological Cooperation Programme Switzerland-Russia for the financial support of the Utilisation of Specific Infrastructure Projects called “Dynamic behaviour of materials for industrial applications”. Russian part of investigations was partially financed by RFBR (Grant 10-01-00585).

#### REFERENCES

1. E. CADONI, A. CAVERZAN and M. DI PRISCO, *Dynamic behaviour of HPFR cementitious composites*, [in:] Ultra-High Performance Concrete, Fehling, Schmidt and Stürwald [Eds.], Proceedings of the 2nd International Symposium on Ultra-High Performance Concrete, Kassel, Heft 10, Structural Materials and Engineering Series, Kassel University Press, 2008, 743–750.
2. A. CAVERZAN, M. COLOMBO and M. DI PRISCO, *High performance steel fibre reinforced concrete: Residual behaviour at high temperature*, [in:] Proceedings of 2nd Workshop on Performance, Protection and Strengthening of Structures under Extreme Loading PROTECT 2009, Hayama, Japan, 2009, on CD ROM.
3. A. CAVERZAN, *High Strain-Rate Uniaxial Tensile Constitutive Behaviour in Fibre Reinforced Cementitious Composites*, Ph.D. Thesis, Politecnico di Milano, 2010.
4. E. CADONI, G. SOLOMOS and C. ALBERTINI, *Mechanical characterization of concrete in tension and compression at high strain-rate using a modified Hopkinson bar*, Magazine of Concrete Research, **61**, 3, 221–230, 2009.
5. E. CADONI, A. MEDA and G. A. PLIZZARI, *Tensile behavior of FRC under high strain-rate*, Materials and Structures, **42**, 9, 1283–1294, 2009.
6. Comité Euro-International du Béton), CEB-FIP Model Code 1990, Redwood Books, Trowbridge, Wiltshire, 1993, UK.
7. A. CAVERZAN, E. CADONI and M. DI PRISCO, *Behaviour of advanced cementitious composites under dynamic loading and fire*, In Proc. of International Workshop on Structures Response to Impact and Blast, Haifa, Israel, 15–17 November 2009.

## ANALYSIS OF LOADS AND STRESSES IN STRUCTURAL ELEMENTS OF HOISTING INSTALLATIONS IN MINES

S. W o l n y, F. M a t a c h o w s k i

**AGH University of Science and Technology**  
**Faculty of Mechanical Engineering and Robotics**

Al. Mickiewicza 30, 30-059 Kraków, Poland

Shaft steelwork-conveyance interactions are present in the literature on the subject available in Poland, these problems have been extensively studied by the research teams from AGH-UST, the Central Mining Institute and the Silesian University of Technology. Despite novel and original solutions in this field, fresh problems tend to appear which have to be solved promptly. In this context an attempt to determine the force of steelwork-conveyance interaction due to irregularities of the guiding string might prove useful in the strength analysis of the conveyance or the shaft steelwork.

This study attempts to determine the steelwork-conveyance interaction force and carrying elements stresses based on the dynamic analysis of the hoist operation, taking into account the irregularities or misalignment of the guiding string and their random occurrence. To validate the model some experiment on a real object were done.

**Key words:** mine hoists, dynamics, loading.

### 1. INTRODUCTION

Conveyances have to be transferred to the shaft landing for the purpose of loading or unloading. This is made possible by the headframe structure which supports the head-gear pulleys and, in some cases, also the winder machine.

The headframe design is chosen depending on the projected functions of the hoist and the shaft, and of the shaft location on the surface. We can have braced structures or hoist towers where the hoists are located in the head gear. The schematic diagram of a hoisting installation with the winder machine placed in a hoist tower is shown in Fig. 1a. Figure 1b shows the schematic diagram of a hoisting installation with the winder installed on the shaft landing.

Nowadays the majority of towered head gears are erected to handle multiple rope hoisting installations only. Apart from the winder mechanisms, their house driving wheels, ventilators, rectifiers or converters. The head structure is also required, to accommodate the guiding systems, fender beams and jack catch devices. Since the multiple-rope towered hoists with pulley blocks have now

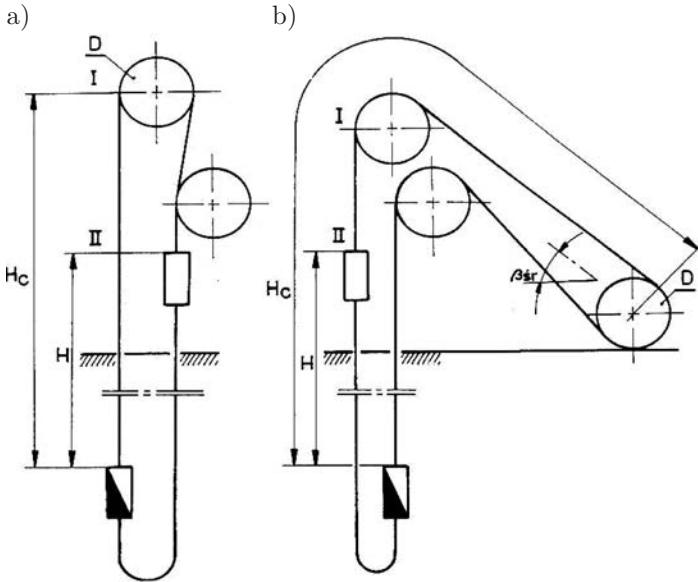


FIG. 1. Schematic diagram of a multiple rope hoisting installation: a) winder in the hoist tower; b) winder on the brink of the shaft.

become the most widespread, this work will be restricted to hoisting installations most popular in our conditions, shown schematically in Fig. 2.

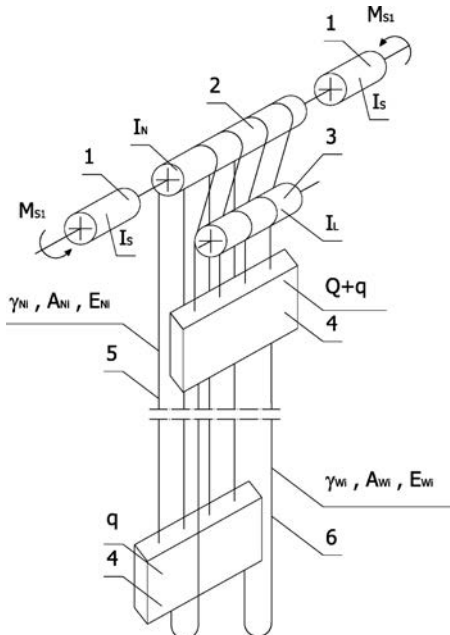


FIG. 2. Schematic diagram of the hoisting installation.

The components of the hoisting installation include:

- 1 – low-torque dc motors, the inertia moment of their armature being  $I_s$ ;
- 2 – multiple rope Koepe pulley of diameter  $D$  and inertia moment  $I_N$ ;
- 3 – deflecting pulleys of the inertia moment  $I_L$ ;
- 4 – skips (conveyances) of the mass  $q$  and loading capacity  $Q$ , the upper skip being loaded;
- 5 – branches of hoisting ropes arranged in parallel, of the rope density  $\gamma_N$  and stiffness under tension  $A_N E_N$ ;
- 6 – branches of tail ropes arranged in parallel, of the rope density  $\gamma_W$  and stiffness under tension  $A_W E_W$ .

Normative standards [1–3] to be applied when designing structural elements of a conveyance (item 4 in the hoist diagram, see Fig. 2) take into account the vertical loads only (loads due to the suspension systems and the tail ropes), whilst the rectilinear vertical motion of the conveyance is disturbed by unevenness of the guide column along which the guide rollers, attached to the conveyance, have to slide. This unevenness (or guide misalignment) gives rise to horizontal forces: the forces of conveyance-shaft steelwork interactions, which are responsible for damaging of the strings connecting the structural components of the conveyance (head, skip hopper, lower frame). So far, many attempts [4–6, 9] have been made to determine those forces, yet the results are still far from satisfactory. In other words, we still lack theoretical relationships defining their value, verified by experiments done on a real object. The authors made a great effort to address this problem, basing on numerical analysis of the FEM model and the results of experiments done on a real object in a colliery in Poland. Furthermore, the authors investigated the state of stress in strings connecting the structural components of the conveyance.

## 2. CONVEYANCE MODEL (FEM 3D)

The numerical model of the conveyance (FEM 3D) was developed, *inter alia*, to find the interaction forces between the conveyance and shaft steelwork and to determine the state of stress and strain in selected elements of the conveyance.

Numerical models of conveyances (FEM 3D) of the lifting capacity 17 Mg (Fig. 3) are based on the technical data of real mine shaft conveyances operated in a colliery in Poland, where the guide misalignment is measured, too.

The numerical model of the conveyance is a beam and surface model, incorporating the following elements (Fig. 4):

- head structure modelled with beam elements;
- skip hopper modelled by beam elements (hopper frame) and by surface elements (hopper panelling);

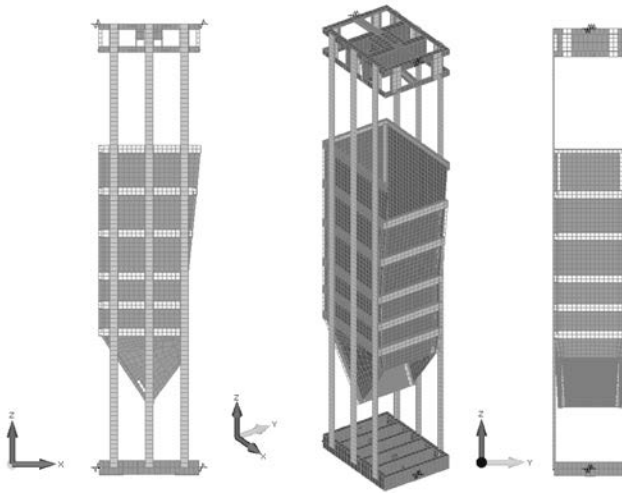


FIG. 3. Numerical (FEM) model of a skip of the lifting capacity 17 Mg.

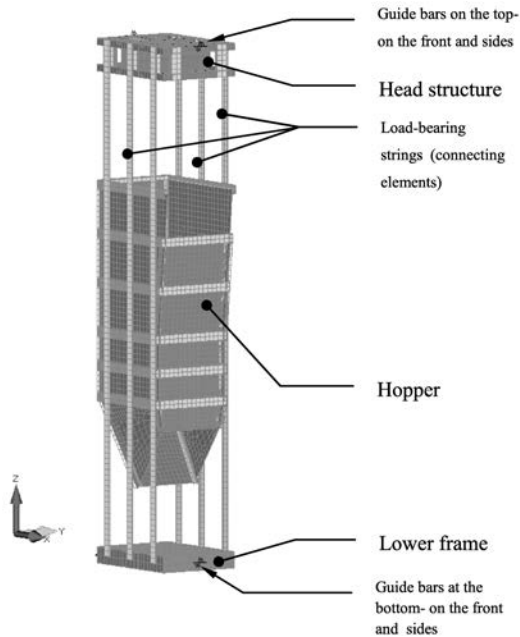


FIG. 4. Structural elements of the skip considered in the FEM model.

- lower frame modelled by beam elements (likewise the head structure);
- load-bearing strings, connecting those three structural components, modelled as beams;
- front and lateral guide bars modelled as elastic-damping elements.

The numerical model (Fig. 4) captures the operating conditions of the mine shaft conveyance. In the vertical direction, the model is supported on the head structure (conveyance suspension) at the attachment point of the hoisting rope thimble (Fig. 5), and at the point where tail ropes (Fig. 6) are attached to the lower frame (tail rope suspension), the time-variant force is applied equivalent to the instantaneous skip loading, due to the weight of tail ropes.



FIG. 5. Attachment of tail ropes for the skip with the support point in the FEM model revealed (red ring).



FIG. 6. Bottom guide bar assembly and attachment of tail ropes.

At the point where the conveyance interacts with the shaft steelwork, the model is supported in the lateral (horizontal) direction via the roller guides systems (on the front and on the sides) by elastic-damping elements, their elasticity and damping factor being equal to relevant elasticity and damping coefficients of the guide bar systems on the front and on the sides (Fig. 7).



FIG. 7. Top guide bar assembly for the skip.

Horizontal displacements of the system during the conveyance travel up and down at the fixed speed  $v$ , are induced by misalignment (irregularities) of the guide column  $x(t)$ , obtained by measurements taken on a real plant. These irregularities impact on the guide bars at the front and on the sides. For the skip travel at the fixed speed  $v$ , it is assumed that the function governing the displacements of the lower guide bars, fixed to the bottom frame  $x(t+\tau)$ , is back-shifted with respect to that governing the displacement of upper guides fixed to the head structure, for the period of time  $\tau = l/v$  equal to that required by the conveyance to travel the distance  $l$  between the upper and lower guide bars (Fig. 8).

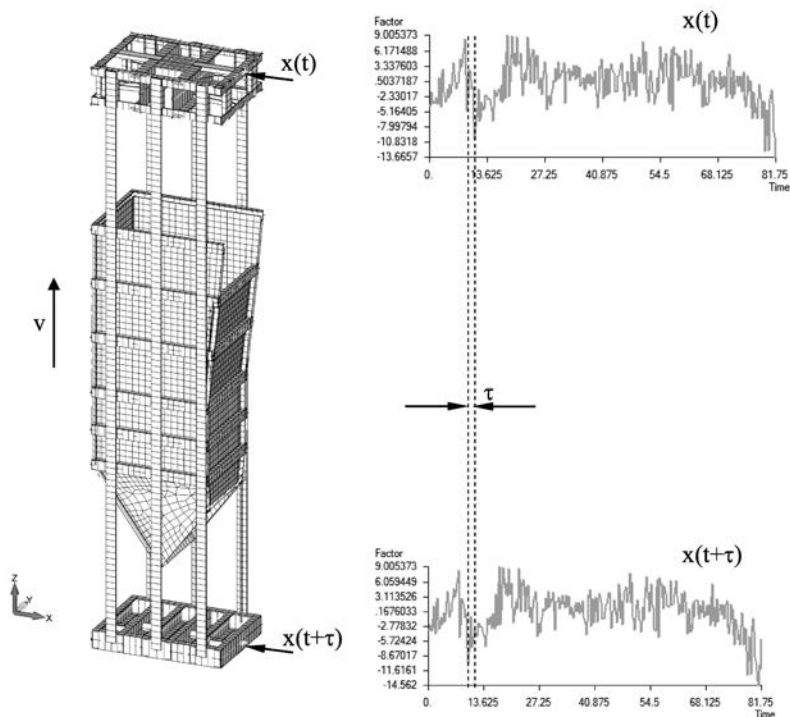


FIG. 8. Schematic diagram of skip loading by the displacement  $x(t)$ .

In numerical analysis we consider a loaded skip, modelled by mass elements (invisible in model diagrams).

### 2.1. Strength analysis

The numerical model of a conveyance is further utilized in the endurance analysis (the state of stress and strain) in structural elements of the system during the full hoisting cycle (loading, hoisting up from the shaft bottom, steady ride, reaching the top station, unloading, ride down of an empty skip). The endurance analysis would yield the conveyance-shaft steelwork interaction forces acting during the conveyance ride at the speed  $v$ . Spectral densities of those forces, are obtained, too.

Figure 9 shows a plot of the conveyance-shaft steelwork interaction forces in the system comprising upper and lower front guide bars (Fig. 10). Plots of conveyance-shaft steelwork interaction forces reveal the maximal values of these forces and their amplitudes. Figure 11 shows the plots of spectral densities of conveyance-shaft steelwork interaction forces (for three hoisting velocities  $v = 12, 16, 20$  m/s), based on the results of the dynamic analysis of the FEM model (FEM 3D).

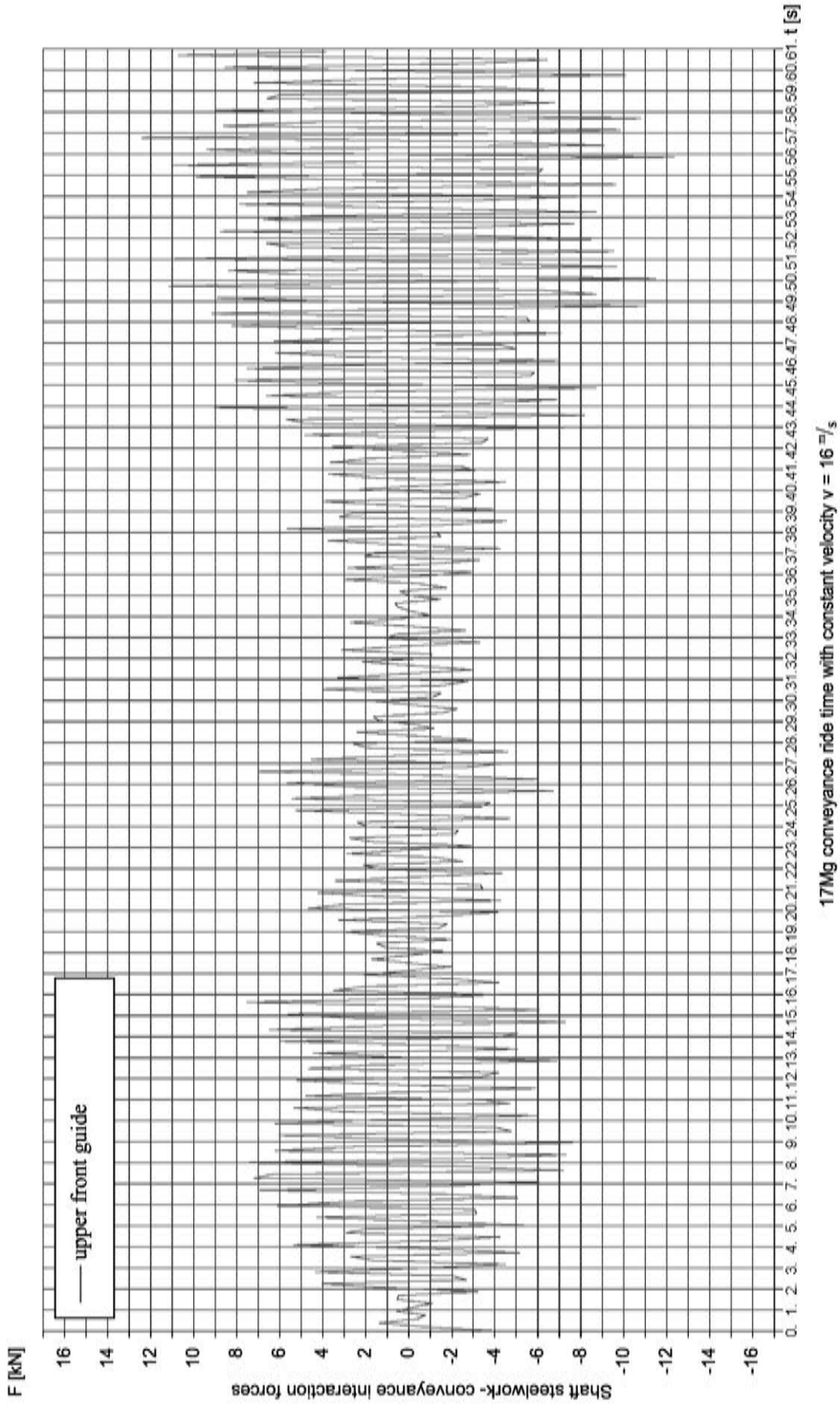


FIG. 9. Shaft steelwork-conveyance interaction forces in the system of upper front guides.

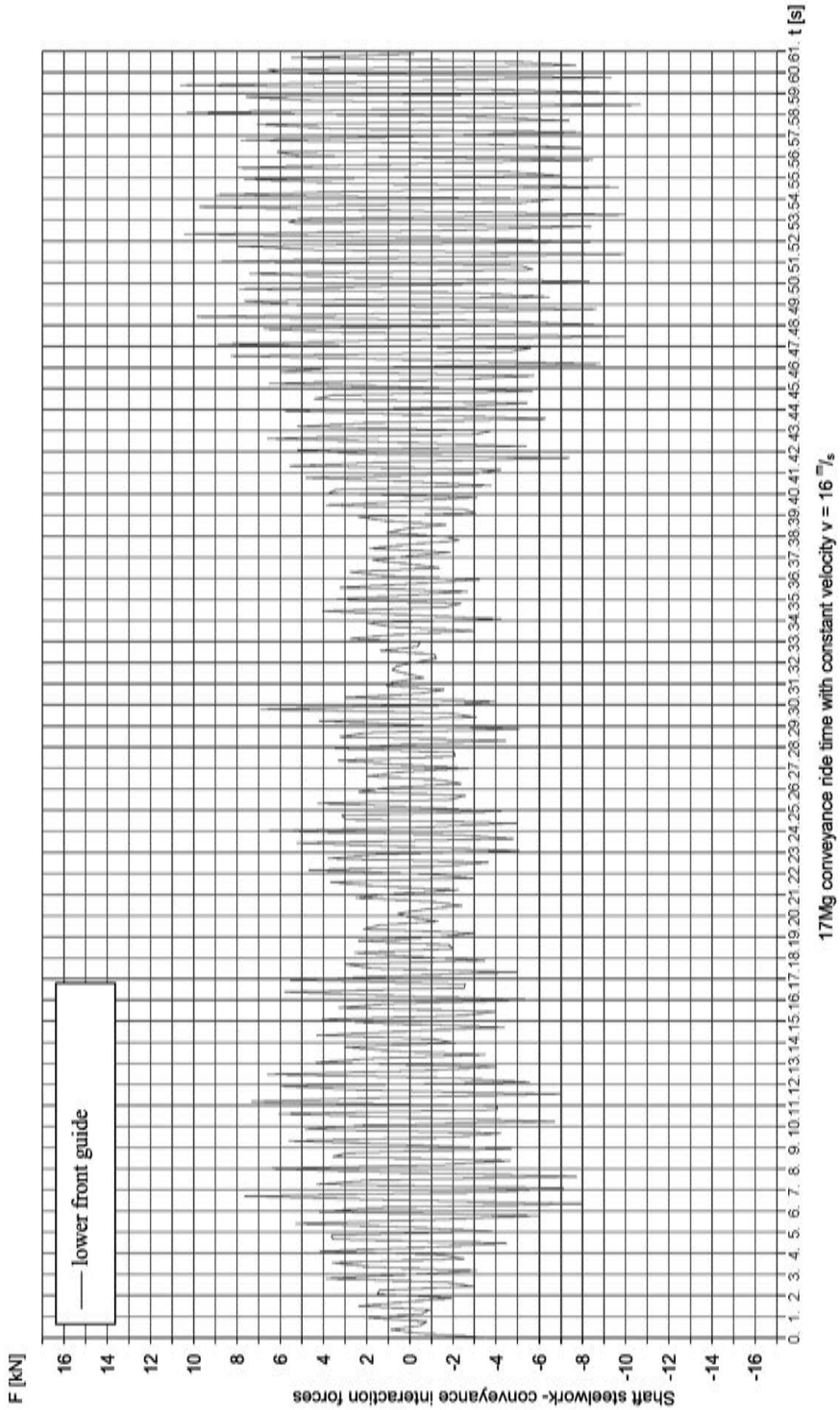


FIG. 10. Shaft steelwork-conveyance interaction forces in the system of lower front guides.

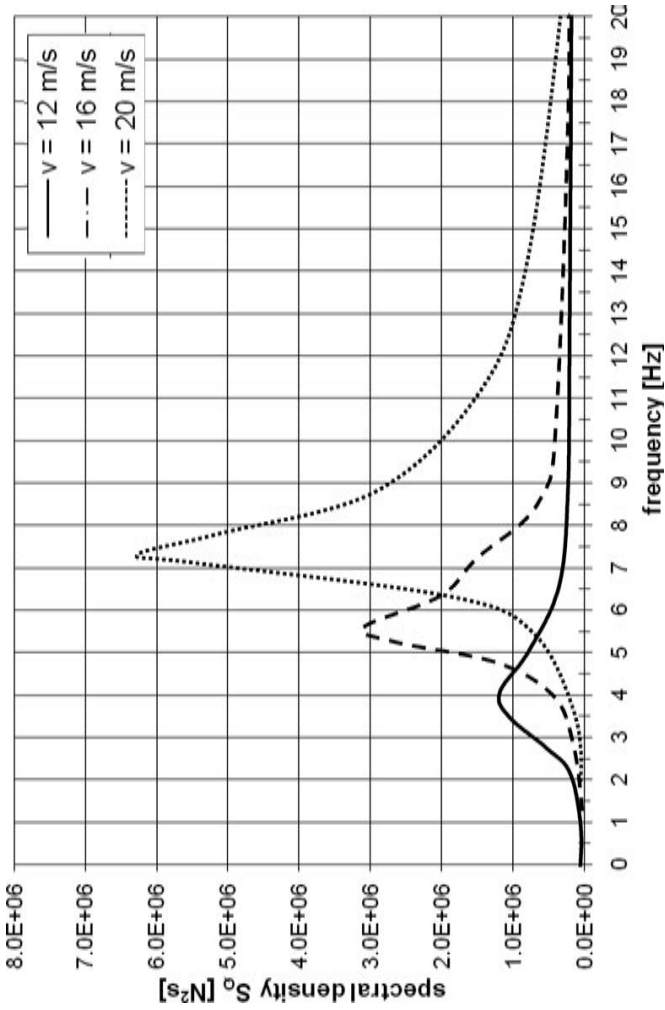


FIG. 11. Spectral densities of conveyance-shaft steelwork interaction forces obtained from solving of the 3D FEM model.

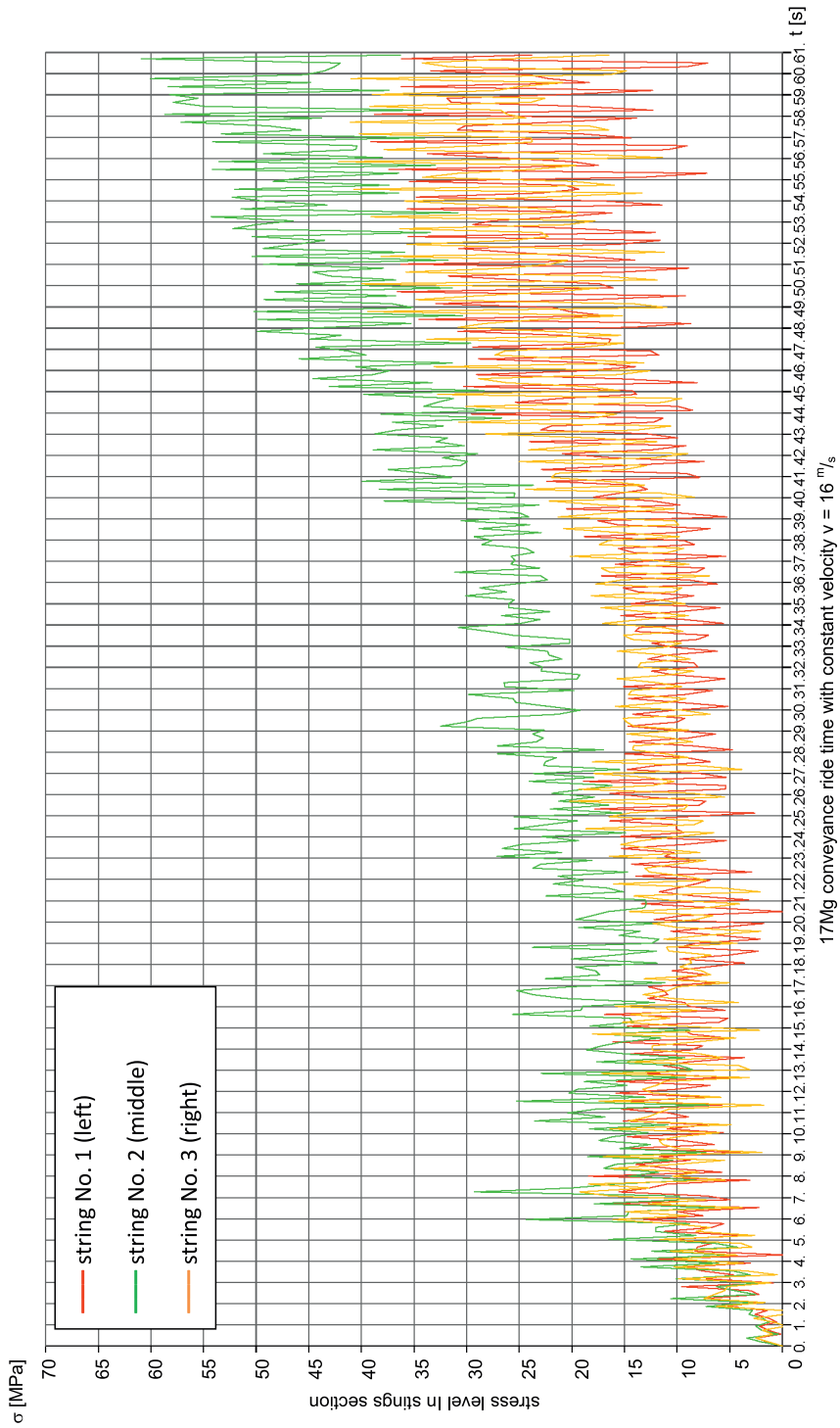


FIG. 12. Normal stresses in string cross-section at the attachment point to the head structure.

Furthermore, the endurance analysis reveals the state of stress in structural elements of the conveyance while it is hoisted from the loading station at the shaft bottom. Figure 12 shows the plots of stresses in cross-sections of strings at their attachment points to the head structure, for the steady ride  $v = 16$  m/s, when the loaded conveyance is hoisted up from the loading station at the bottom.

### 3. EXPERIMENTS ON A REAL OBJECT

Roller guides (Fig. 13) in hoisting installations are used to guide a conveyance along the vertical guides in the shaft. Therefore they have to transmit the conveyance-shaft steelwork interaction forces. Deformation of elastic elements of the roller guide might be used to determine the extent of this interaction.



FIG. 13. Roller guide assembly- at the bottom.

Figure 14 shows the schematic diagrams of the front roller guide mechanism (Fig. 14a) and of the lateral guide (Fig. 14b), being the elements of the tested hoist. To determine the shaft steelwork-conveyance interaction forces, we recall the procedure of measuring of the displacement  $X_2$  (displacement of the roller housing with respect to the guide bar, permanently fixed to the head structure, lower frame) of the conveyance (Fig. 14).

The formula governing the load acting upon the front and lateral roller guide system, as a function of its displacement  $X_2$  and the displacement  $X_2$  is derived, basing on laboratory data for various types of guide bar systems summarized in the papers [7].

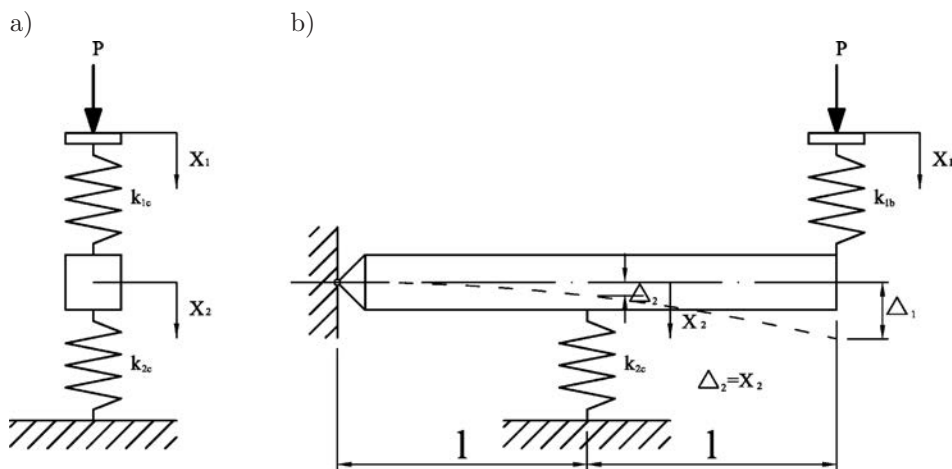
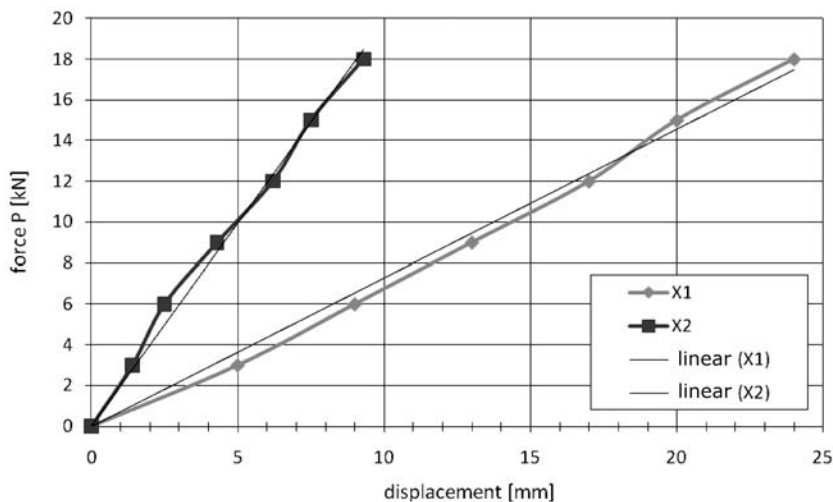


FIG. 14. Diagrams of the roller guide systems: a) front; b) lateral.

Figure 15 shows the static characteristic of the front roller guide (loading force  $P$  vs. the total displacement  $X_1$ , the displacement  $X_2$  being simultaneously registered). The static characteristic of the lateral guide is given in Fig. 16. In both cases, the indicated linearized characteristics  $P(X_1)$  and  $P(X_2)$  agree well with those obtained experimentally.

Measurements of displacement ( $X_2$  in Fig. 15a) were taken with induction sensor and strain gauges attached to the measuring beam, in a device fabricated especially for the purpose of the research program [7].

FIG. 15. Static characteristic of the front roller guide obtained by measurements ( $X_1$  – total displacement;  $X_2$  – displacement of the roller housing) and its linearized form.

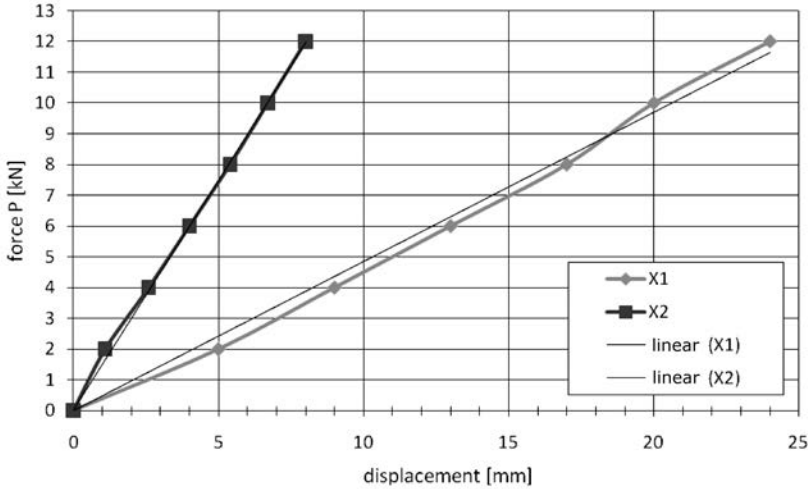


FIG. 16. Static characteristic of the lateral roller guide obtained by measurements ( $X_1$  – total displacement;  $X_2$  – displacement of the roller housing) and its linearized form.

The data obtained from periodic overhauls of skips and cages operated in Polish mines indicate that a majority of the reported conveyance failures are caused by fatigue cracking [6]. These cracks appear and propagate mostly in load-bearing strings or in welded sections, in the areas where they are attached to the conveyance structure. In order to find the real value of stress in the areas where fatigue cracks are registered, measurements are taken with strain gauges in the service conditions.

Measurements of the conveyance-shaft steelwork interaction force are taken for the hoisting installation, in which the guide misalignment was measured (lifting capacity  $Q = 17$  Mg, hoisting distance  $H = 1020$  m, hoisting speed 16 m/s).

The measurements covered a full cycle of skip operations:

1. Ride down to the charging station (on the shaft bottom);
2. Loading (17 Mg);
3. Hoisting of a loaded skip to the shaft top;
4. Unloading at the shaft top.

Measurements were taken during three consecutive full cycles of skip operation. Figure 17 shows the arrangement of measuring sensors and numbering of relevant guide bars. Measurements covering the full cycle of skip operations were repeated three times. Figure 18 shows the strain gauge fixed to the upper front roller guide and Fig. 19 shows the induction sensors attached to the lower guide assembly. Figure 20 shows the plots of measured displacements of the guiding elements in the front roller guide.

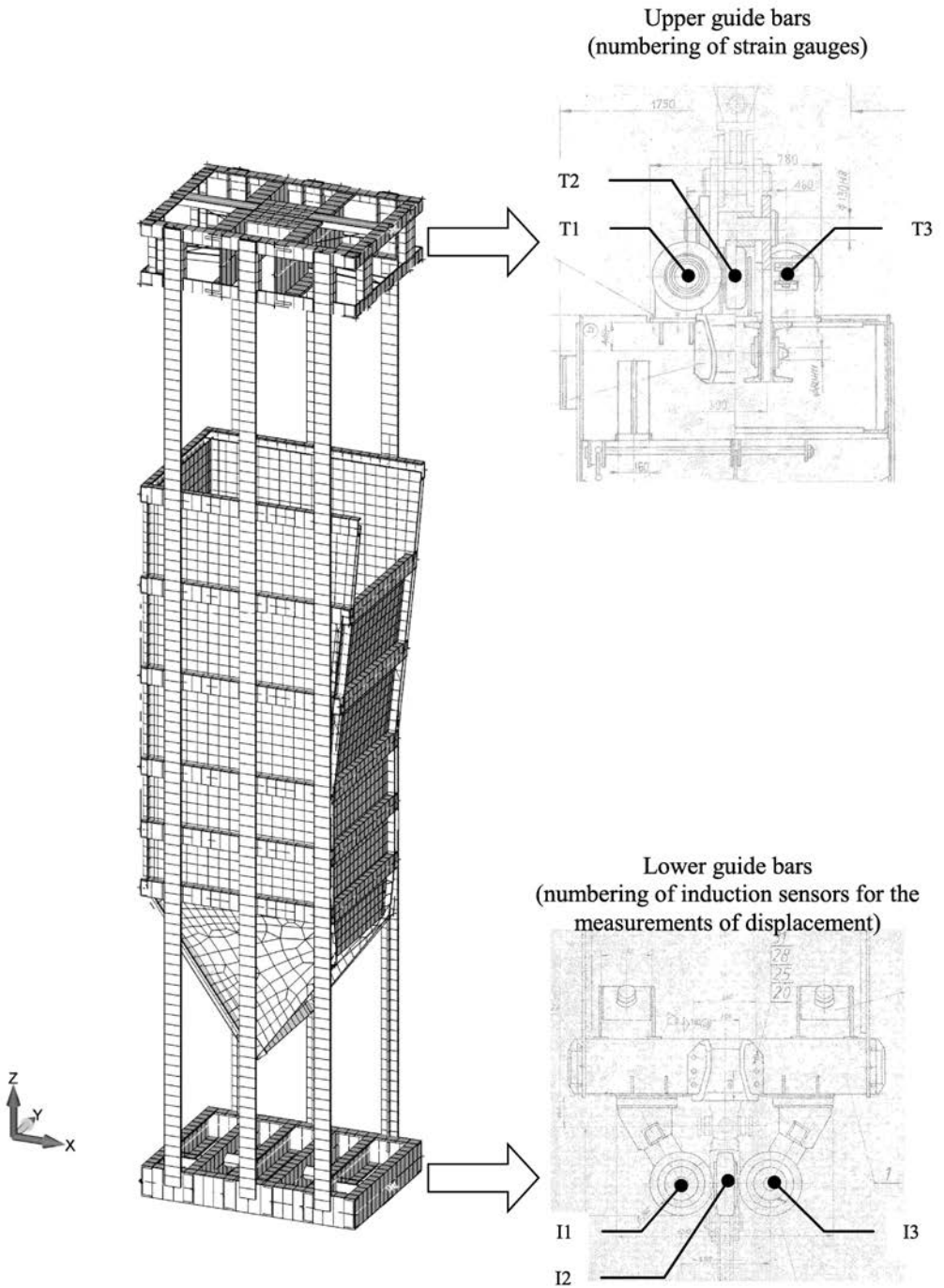


FIG. 17. Configuration and numbering of measurement points.

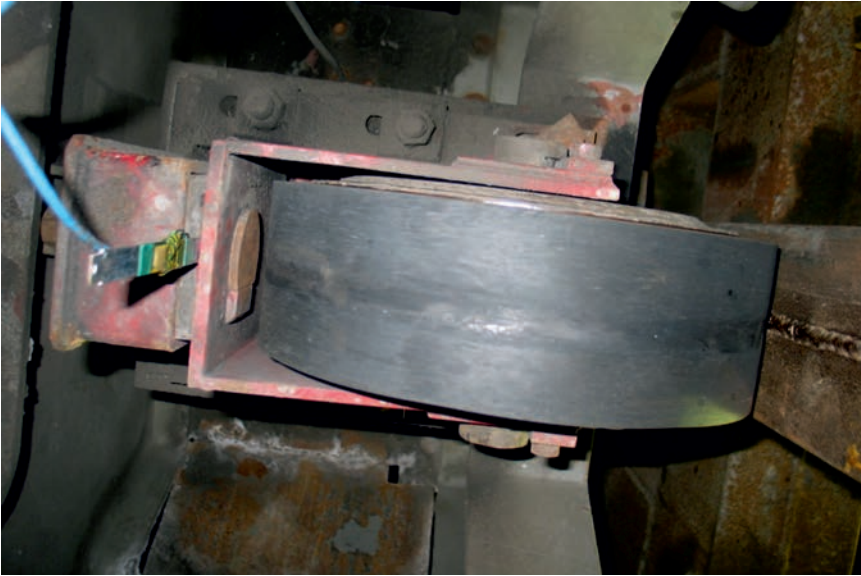


FIG. 18. Upper front guide with an attached strain gauge, general view.



FIG. 19. Lower roller guide assembly with the attached induction sensors.

Measured displacements in the conveyance guiding system in conjunction with the roller guide characteristic (Figs. 15, 16), yield the maximal shaft steel-work-conveyance interaction forces in the system comprising front roller guides on the top (fixed to the head structure) and at the bottom (fixed to the lower frame). The results are compiled in Table 1.

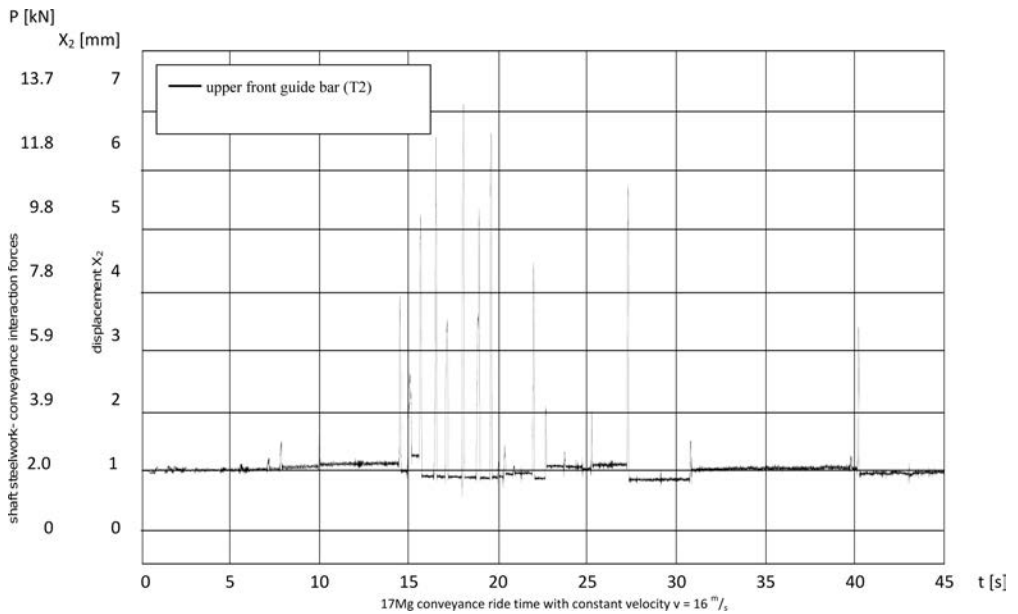


FIG. 20. Registered displacement  $X_2$  of the upper front guide bar (Travel I) during the ride up of a loaded conveyance.

**Table 1. Maximal shaft steelwork-conveyance interaction forces.**

Cycle	Phase	Upper roller guide assembly			Bottom roller guide assembly		
		Side left $P_{bl}$ [kN]	Front $P_c$ [kN]	Side right $P_{br}$ [kN]	Side left $P_{bl}$ [kN]	Front $P_c$ [kN]	Side right $P_{br}$ [kN]
I	Ride down (empty)	1.7	2.4	1.6	2.0	0.8	0.2
	Loading	1.4	2.0	2.2	1.0	0.2	0.1
	Ride up (loaded)	3.4	12.8	9.2	1.7	9.0	0.6
	Unloading	0.2	0.8	0.4	0.2	0.2	0.4
II	Ride down (empty)	0.6	2.6	6.0	2.2	1.0	0.5
	Loading	0.8	1.0	0.8	0.4	0.4	0.5
	Ride up (loaded)	4.8	12.0	14.0	2.3	7.6	0.6
	Unloading	0.1	0.4	0.3	0.1	0.4	0.4
III	Ride down (empty)	0.6	1.2	6.0	2.0	0.6	0.4
	Loading	0.9	0.4	0.4	0.4	0.6	0.4
	Ride up (loaded)	4.6	11.8	11.8	2.0	6.6	0.6
	Unloading	0.1	0.4	0.8	0.3	1.0	0.3

Basing on experimental data, the plots of spectral density of maximal shaft steelwork-conveyance interaction forces are obtained for the conveyance travel at the fixed speed  $v = 16$  m/s during the test. Figure 21 shows the plots of spectral density of the interaction force  $S_Q$ :

- black colour – spectral density of force obtained from solving the FEM model,
- red colour – spectral density of force obtained from measurements on a real object.

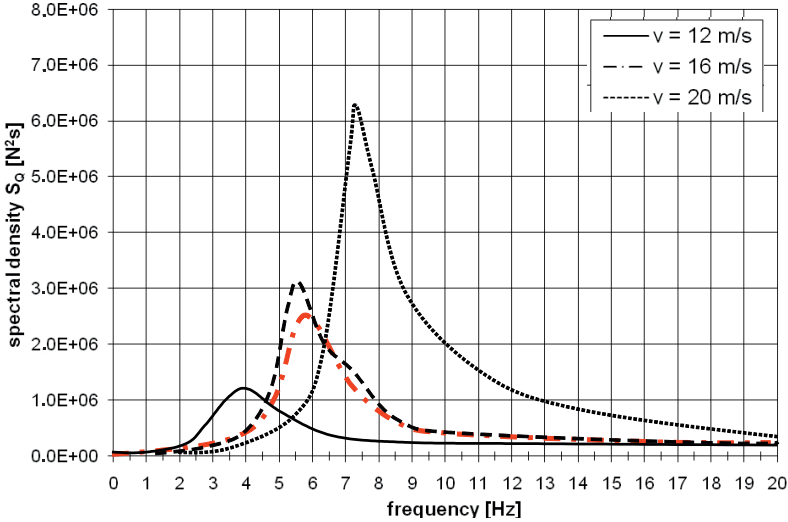


FIG. 21. Spectral densities of “shaft steelwork-conveyance interaction” forces obtained by solving of the 3D FEM model and experimentally (red colour).

Measurements in the load-bearing strings of the conveyance are restricted to stress concentration, revealed by the endurance analysis.

Strain gauges designated as TC1, TC2, TC3, TC4 are attached to the string on the head structure, as shown in Figs. 22 and 23. The sensors TC5, TC6, TC7, TC8 are fixed on the strings beneath the first frame of the hopper (Figs. 24, 25). Sensors TC5 and TC5', TC6 and TC6', TC7 and TC7', TC8 and TC8' are fixed to the opposite surfaces of the strings in the half-bridge configuration and connected to relevant measurement channels. This arrangement allows for measuring of this part of stress which is due to the bending moment acting in the plane perpendicular to that, to which the strain gauges are fixed. Strain gauges are placed at the distance of 135 mm from the lower edge of the frame, and the strain gauge 9 – at the distance of 35 mm from this frame.

Figure 26 shows the stresses measured in the string cross-section throughout the full cycle of skip operation. It is worthwhile to mention that the sensors were attached in the tower structure, at the instant when the loading due to tail ropes should be the greatest. That is why the plot reveals 26 compressive stresses not experienced in real service, registered in the initial phase of the ride down and ride up. Therefore, the whole plot should be shifted ‘upwards’ by the value of the smallest measured stress (as given in Table 2).

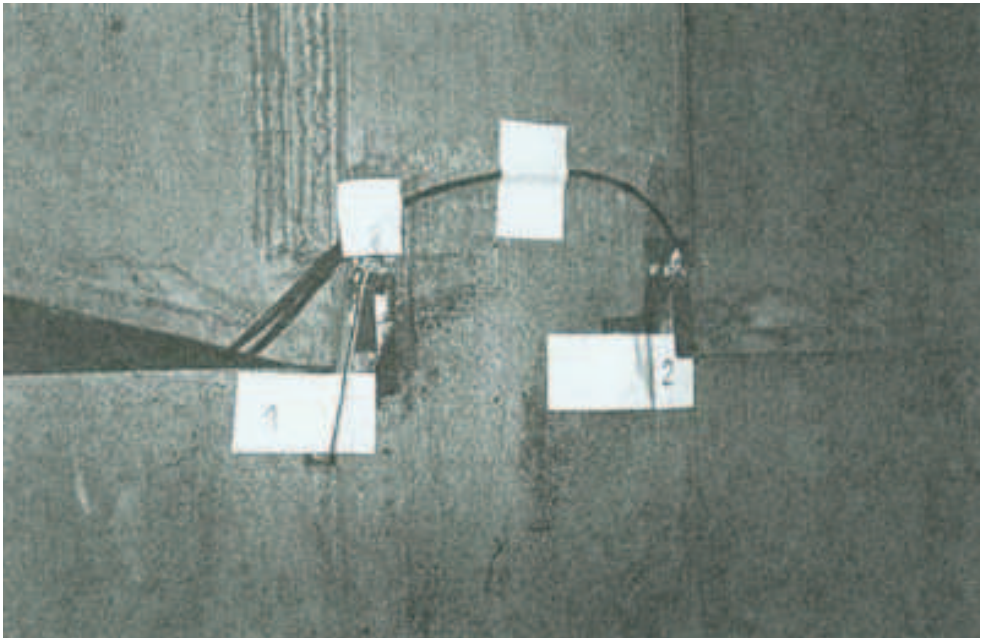


FIG. 22. Strain gauges TC1 and TC2 fixed to the left-side string, at the attachment point to the head structure.



FIG. 23. Strain gauges TC3 and TC4 fixed to the mid-point string, at the attachment point to the head structure.



FIG. 24. Sensors TC5, TC5', TC6, TC6' fixed at the point where the mid-point string is connected with the hopper structure.

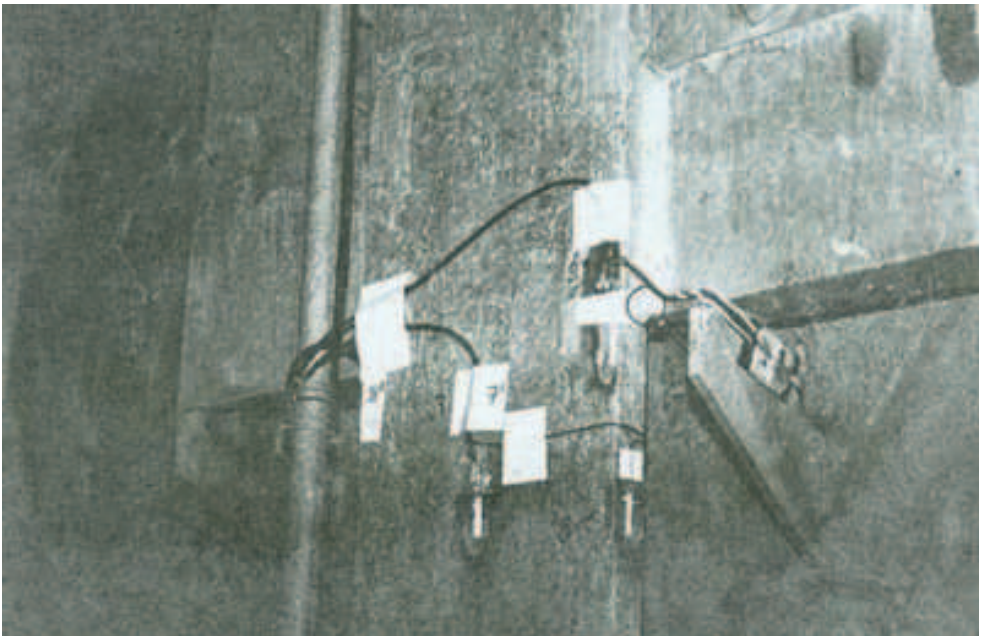


FIG. 25. Sensors TC7, TC7', TC8, TC8' and TC9, fixed at the point where left-side string is connected with the hopper structure.

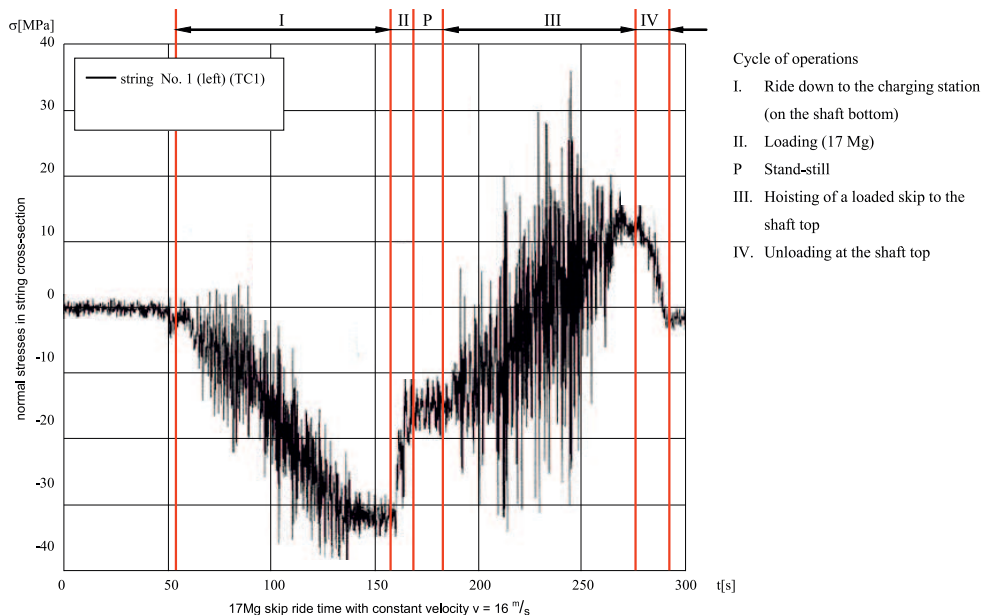


FIG. 26. Stress in the string cross-section registered by the sensor TC1.

The maximal stresses and their amplitudes are compiled in Table 2 for each cycle of operation, and compared with the FEM model solutions.

**Table 2. Maximal stresses and their amplitudes in string cross-sections obtained experimentally, for the ride up of the loaded conveyance at the speed  $v = 16 \text{ m/s}$ .**

Cycle	Left-side string				Middle string			
	Attachment point to the skip head structure TC1, TC2		Attachment point to the hopper frame TC7, TC8, TC9		Attachment point to the skip head structure TC1, TC2		Attachment point to the hopper frame TC7, TC8, TC9	
	max. [MPa]	ampl. [MPa]	max. [MPa]	ampl. [MPa]	max. [MPa]	ampl. [MPa]	max. [MPa]	ampl. [MPa]
I	68	45	75	43	62	38	71	41
II	69	43	79	44	63	38	72	42
III	68	46	76	43	61	38	71	42
MES	43	22	45	26	62	43	63	43

#### 4. CONCLUSIONS

The shaft steelwork-conveyance interaction forces and stresses, measured in strings connecting the structural elements of the conveyance, agree well with numerical FEM solutions (3D FEM model).

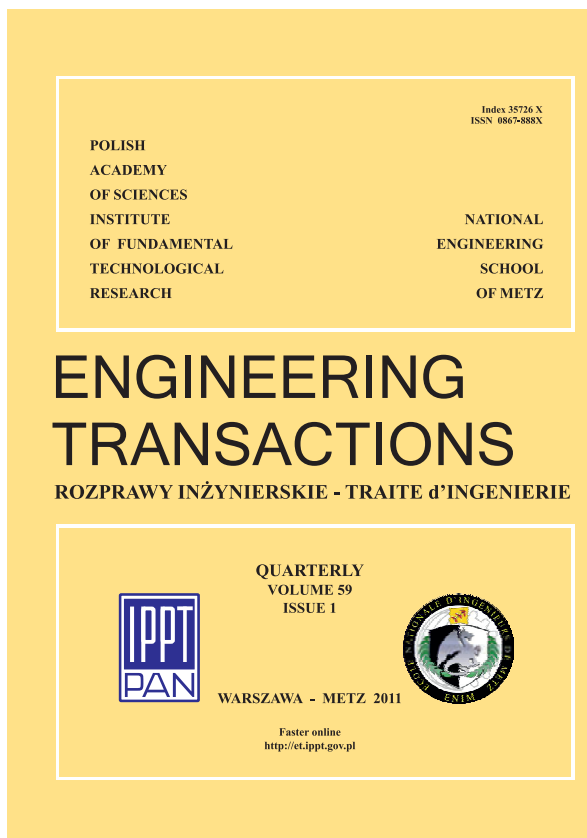
Stresses are measured in load-bearing strings; the extreme and the middle ones, are very similar, whilst stresses obtained by the FEM analysis (the solution for three strings) would significantly differ. One has to bear in mind, however, that the FEM model was developed basing on the technical specification data of the machine, so it fails to take into account the stress experienced during the assembly procedures and the ‘adjustment’ of the structure to the operating conditions. These factors prove to be major determinants of stress distribution in load-bearing strings.

The analysis of shaft steelwork-conveyance interactions due to misalignment of the guide column and their influence on stresses experienced in structural elements of the conveyance, can become a starting point for defining the fatigue endurance of load-bearing components of the conveyance. Furthermore, this study can be utilised in optimisation of structural parameters of the system (mass, fatigue endurance).

#### REFERENCES

1. *Regulation of Economy Minister from 28 June 2002 on safety and occupational health* [in Polish], Dz.U. Nr 139, poz. 1169.
2. *Regulation of Economy Minister from 9 June 2006 on safety and occupational health* [in Polish], Dz.U. Nr 124, poz. 863.
3. *Regulation of The Council of Ministers from 30 April 2004 on acceptance of products for use in mining* [in Polish], Katowice, 2006.
4. S. KAWULOK, *Influence of elasticity of mining vessel on its dynamics* [in Polish], Katowice, Biuletyn GIG, **2**, 94, 1987.
5. D. TEJSZERSKA, *Modeling of coupled transverse-longitudinal vibration of mining vessel system* [in Polish], Gliwice: Wyd. Politechniki Śląskiej, 1995.
6. M. PŁACHNO, *Method of measurement and analysis of mining vessel transversal vibration useful to appoint of real vessel and steel works loads* [in Polish], Kraków, Zeszyty Naukowo-Techniczne KTL, **15**, 1999.
7. S. WOLNY, *Dynamic Loading of the Pulley Block In a Hoisting Installation In Normal Operating Conditions*, Archives of Mining Sciences, **54**, 2, 261–284, 2009.
8. S. WOLNY, *Analysis of Loading in the Conveyance – Shaft Steelwork System*, Archives of Mining Sciences, **51**, 4, 529–546, 2006.
9. S. WOLNY, F. MATACHOWSKI, *Operating loads of the shaft steelwork-conveyance system due to random irregularities of the guiding strings*, Archives of Mining Sciences, **55**, 3, 589–603, 2010.

Starting from the year 2011, the Quarterly Journal *ENGINEERING TRANSACTIONS* will be published jointly with the National Engineering School of Metz – ENIM (France) under the new French-Polish Editorial Committee chaired by two editors: R. Pęcherski and A. Rusinek.



# ENGINEERING TRANSACTIONS **Appears since 1952**

Copyright ©2010 by Institute of Fundamental Technological Research,  
Polish Academy of Sciences, Warsaw, Poland

## **Aims and Scope**

ENGINEERING TRANSACTIONS promotes research and practise in engineering science and provides a forum for interdisciplinary publications combining mechanics with material science, electronics (mechanotronics), medical science and biotechnologies (biomechanics), environmental science, photonics, information technologies and other engineering applications. The Journal publishes original papers covering a broad area of research activities including experimental and hybrid techniques as well as analytical and numerical approaches. Engineering Transactions is a quarterly issued journal for researchers in academic and industrial communities.

## INTERNATIONAL COMMITTEE

S. A. ASTAPCIK (*Byelorussia*)  
G. DOBMANN (*Germany*)  
JI-HUAN HE (*China*)  
M. N. ICHCHOU (*France*)  
W. JÜPTNER (*Germany*)  
A. N. KOUNADIS (*Greece*)

P. KUJALA (*Finland*)  
J. LIN (*U.K.*)  
G. PLUVINAGE (*France*)  
V. V. SKOROKHOD (*Ukraine*)  
P. C. B. TSAY (*Taiwan*)  
Z. WESOŁOWSKI (*Poland*)

## EDITORIAL COMMITTEE

L. DIETRICH – **Editor**  
B. GAMBIN  
K. KOWALCZYK-GAJEWSKA  
Z.L. KOWALEWSKI  
B. LEMPKOWSKI – secretary

J. HOLNICKI-SZULC  
R. PEŁCHERSKI

Address of the Editorial Office:  
Engineering Transactions  
Institute of Fundamental Technological Research  
Pawińskiego 5B,  
PL 02-106 Warsaw, Poland

Phone: (48-22) 826 60 22, Fax: (48-22) 826 98 15, E-mail: publikac@ippt.gov.pl

## **Abstracted/indexed in:**

Applied Mechanics Reviews, Current Mathematical Publications, Inspec, Mathematical Reviews, MathSci, Zentralblatt für Mathematik.

<http://et.ippt.gov.pl/>

# SUBSCRIPTIONS

Address of the Editorial Office: Engineering Transactions

Institute of Fundamental Technological Research

Pawińskiego 5B, PL 02-106 Warsaw, Poland

Tel.: (48-22) 826 60 22, Fax: (48-22) 826 98 15, E-mail: publikac@ippt.gov.pl

**Subscription orders for all journals edited by IPPT (Institute of Fundamental Technological Research) may be sent directly to the Publisher:  
Institute of Fundamental Technological Research  
e-mail: subscribe@ippt.gov.pl**

Please transfer the subscription fee to our bank account: Payee: IPPT PAN,  
Bank: Pekao S.A. IV O/Warszawa,  
Account number 05124010531111000004426875.

All journals edited by IPPT are available also through:

- Foreign Trade Enterprise ARS POLONA ul. Obrońców 25,  
03-933 Warszawa, Poland, Tel. (48-22) 509 86 38, 509 86 37  
e-mail: arspolona@arspolona.com.pl
- RUCH S.A. ul. Jana Kazimierza 31/33,  
01-248 Warszawa, Poland,  
Tel. (48-22) 532 88 16, Fax (48-22) 532 87 31  
e-mail: prenumerata@okdp.ruch.com.pl
- International Publishing Service Sp. z o.o. ul. Noakowskiego 10 lok. 38  
00-664 Warszawa, Poland, Tel./fax: (48-22) 625 16 53, 625 49 55  
e-mail: books@ips.com.pl

---

## Warunki prenumeraty

**Prenumeratę na wszystkie czasopisma wydawane przez IPPT PAN przyjmuje Dział Wydawnictw IPPT. Bieżące numery można nabywać, a także zaprenumerować roczne wydanie Engineering Transactions, bezpośrednio w IPPT PAN, ul. Pawińskiego 5B, 02-106 Warszawa**

**Tel.: (48-22) 826 60 22; Fax: (48-22) 826 98 15**

**e-mail: subscribe@ippt.gov.pl**

Czasopisma można zamówić (przesyłka za zaliczeniem pocztowym) w Warszawskiej Drukarni Naukowej PAN, ul. Śniadeckich 8, 00-656 Warszawa

Tel./Fax (48-22) 628 87 77; (48-22) 628 76 14, e-mail: dystrybucja@wdnpan.pl

Wpłaty na prenumeratę przyjmują także regionalne Działy Sprzedaży Prasy RUCH S.A.

Infolinia: 804 200 600. Zamówienia można przysłać pocztą elektroniczną ze strony

www.prenumerata.ruch.com.pl

---

Arkuszy wydawniczych 6.50; Arkuszy drukarskich 5.25

Papier offset. kl. III 70 g. B1

Skład w systemie L<sup>A</sup>T<sub>E</sub>X K. Jezierska

Druk i oprawa: Drukarnia Braci Grodzickich, Piaseczno ul. Geodetów 47A

---